*J. Fluid Mech.* (2020), *vol.* 882, A29. © Cambridge University Press 2019
doi:10.1017/jfm.2019.839


# An analytical correction to Amiet's solution of airfoil leading-edge noise in non-uniform mean flows

**Siyang Zhong**[1,2,†], **Xin Zhang**[1,3,†], **Bo Peng**[1] **and Xun Huang**[4,1]

[1]Department of Mechanical and Aerospace Engineering, Hong Kong University of Science and Technology, Hong Kong, PR China

[2]Institute for Advanced Study, Hong Kong University of Science and Technology, Hong Kong, PR China

[3]HKUST–Shenzhen Research Institute, Shenzhen, PR China

[4]State Key Laboratory of Turbulence and Complex Systems, Department of Aeronautics and Astronautics, College of Engineering, Peking University, Beijing, PR China

(Received 8 March 2019; revised 29 September 2019; accepted 13 October 2019)

Gust/turbulence–leading edge interaction is a significant source of airfoil broadband noise. An approach often used to predict the sound is based on Amiet's flat-plate solution. Analytical studies have been conducted to investigate the influences of airfoil geometries, non-uniform mean flows and turbulence statistics, which, however, were often too convoluted. In this work, the problem is revisited by proposing simple corrections to the standard flat-plate solution to account for the effect of non-uniform mean flows of real airfoils. A key step in the method is to use a new space–time transformation that is analogous to the Prandtl–Glauert transformation to simplify the sound governing equation with spatially varying coefficients to a classical wave equation, which is then solved using the Schwarzschild technique as in Amiet's solution. The impacts of Mach number, wavenumber and airfoil geometry on the prediction accuracy are investigated for both single-frequency and broadband cases, and the results are compared against high-fidelity simulations. It predicts the sound reduction by the airfoil thickness, and reveals that the reduction is caused by the non-uniform streamwise velocity. The limitations of the model are discussed and the approximation errors are estimated. In general, the prediction error increases with the airfoil thickness, the sound frequency and the flow Mach number. Nevertheless, in all cases studied in this work, the proposed correction can effectively improve the prediction accuracy of the flat-plate solution much more efficiently compared to numerical solutions of the Euler equations using computational aeroacoustics.

**Key words:** aeroacoustics

## 1. Introduction

The regulatory requirements to reduce the impacts of aircraft operation are becoming more stringent with the rapid growth of global aviation. During the

† Email addresses for correspondence: zhongsy@ust.hk, aexzhang@ust.hk

approach-to-landing and take-off phases of aircraft operation, the engines are the major source of aircraft noise (Magliozzi 1991), in which the leading-edge noise caused by fan wakes interacting with outlet guide vanes in turbofan engines or aft rotor blades in contra-rotating open rotors is significant. Turbulent gusts are convected by the mean flow from the upstream of the rotor/fan blades, and produce broadband noise when they experience significant distortions due to the blockage effect of the downstream outlet guide vanes or rotor blades. For the analytical prediction of the leading-edge noise, the flat-plate solution proposed by Amiet (1975, 1976*a*, 1989) is widely used (Node-Langlois *et al.* 2014). In the model, the background mean flow is uniform, and the governing equation for sound is the convected wave equation. Different mathematical techniques such as matched asymptotic expansion, the Schwarzschild technique and the Wiener–Hopf methods have been adopted to solve the equation, and the associated theoretical background dates back to early studies in aerodynamics of unsteady airfoil theory by von Kármán & Sears (1938) and Sears (1938) and the unsteady transonic flow theory by Landahl (1989).

By using simple physical concepts of circulation theory, von Kármán & Sears (1938) computed the aerodynamic load, momentum and lift of an unsteady thin airfoil. Sears (1941) showed that the motion of the unsteady theory is equivalent to a stationary flat plate interacting with incompressible incoming gusts. For sinusoidal gusts, Kemp (1952) showed that the transfer function between the aerodynamic force and the gust upwash velocity is related to the Sears' function. However, the application of the theory to practical aeroacoustics problems should resolve the issue of the compressibility effect (Atassi 1984), i.e. the motions of the fluctuation variables in the von Kármán and Sears' solutions are governed by the Laplace equation while in practice they are governed by the convected wave (Helmholtz) equation. Corrections to the incompressible results were made by Miles (1950), Amiet & Sears (1970) and Osborne (1973) to transform the governing equation to a classical wave equation. Under a low-frequency assumption, the unsteady pressure is obtained from the inner solution (of the matched asymptotic expansion method) based on the incompressible unsteady airfoil theory (von Kármán & Sears 1938; Sears 1938). A further contribution was made by Amiet (1974) to remove the 'anomalous behaviour' due to the incorrect velocity condition applied at the airfoil trailing edge (Amiet 1976*b*) in the previous works (Miles 1950; Amiet & Sears 1970; Osborne 1973).

However, at high frequency, it is hard to define an inner region where the gusts could be viewed as incompressible. Fortunately, in this case, the value of the chord–wavelength ratio is large, which enables separate treatment of the leading-edge and trailing-edge effects. The mathematical techniques that are suitable for partial differential equations with semi-infinite boundary conditions can then be employed. Adamczyk (1974) computed the pressure response using the Wiener–Hopf method for both two-dimensional (2-D) compressible and three-dimensional (3-D) incompressible cases. The solution was generalised by Amiet (1976*a*) using the Schwarzschild technique (Schwarzschild 1901). The essential idea is that the induced sound field due to the singularity at the leading edge should cancel the upwash velocity of the incoming gust (as required by the hard-wall condition on the airfoil surface). A zeroth-order solution $\phi^{(0)}$ is first constructed using the Green's function method. However, the hard-wall condition is only valid on the surface $x_1 \in (0, c)$, where $c$ is the flat-plate chord length. The key measure of the solution is firstly to propose a leading-edge correction $\psi^{(1)}$ by solving the Helmholtz equation (or wave equation) with two-section semi-infinite boundary conditions: $\psi^{(1)}(x_1) = -\phi^{(0)}(x_1)$ for $x_1 < 0$, and $\partial\psi^{(1)}/\partial x_2 = 0$ for $x_1 > 0$. The solution to this problem is obtained by using

the Schwarzschild technique, and the solution $\phi^{(1)} = \phi^{(0)} + \psi^{(1)}$ meets the boundary conditions that $\phi = 0$ for $x_1 < 0$ and $\partial\phi/\partial n = -\boldsymbol{v}_g \cdot \boldsymbol{n}$ for $0 \leqslant x_1 \leqslant c$. The same strategy is applied to the trailing-edge correction to cancel the pressure fluctuation induced by $\phi^{(1)}$ in the wake region (such that $p' = 0$ for $x_1 > c$) to meet the Kutta condition. The two corrections are often referred to as leading-edge scattering and trailing-edge back-scattering (Roger & Moreau 2010; Blandeau *et al.* 2011). The procedures for introducing corrections at the edges were also adopted by Martinez & Widnall (1980), who employed the Wiener–Hopf method to tackle the problem. A unified solution that combined the low-frequency and high-frequency responses was given by Amiet (1989).

Amiet's solution was initially validated by wind tunnel measurements of grid-generated turbulence interacting with a flat plate (Paterson & Amiet 1977), and by computational aeroacoustics (CAA) with thin airfoils (Gill, Zhang & Joseph 2013). However, the flat-plate solution suffers from limitations of oversimplifying the airfoil geometry and ignoring the non-uniform mean flow effects. Many numerical, experimental and theoretical studies have been conducted to investigate the impact of these factors. The main conclusions are that the airfoil leading-edge noise can be greatly reduced by the airfoil thickness at high frequencies (Olsen & Wagner 1982; Glegg, Baxter & Glendinning 1987; Atassi, Subramaniam & Scott 1990; Lockard & Morris 1998; Guidati & Wagner 1999; Gershfeld 2004; Oerlemans & Migliore 2004; Devenport, Staubs & Glegg 2010; Roger & Moreau 2010; Hall *et al.* 2011; Gill *et al.* 2013), while the sound radiation is insensitive to the airfoil angle of attack and camber in isotropic turbulent flows (Paterson & Amiet 1977; Moreau, Roger & Jurdic 2005; Moriarty, Guidati & Migliore 2005; Staubs 2008; Devenport *et al.* 2010; Gill *et al.* 2013). The acoustic properties of transonic airfoils with shocks were investigated by Zhong *et al.* (2017, 2018, 2019).

As for extensions to the flat-plate solution, Gershfeld (2004) developed a correction method by using a modified Green's function, in which an exponentially decaying term was employed to account for the sound reduction by airfoil thickness. Moreau *et al.* (2005) development a semi-empirical analytical correction based on the rapid distortion theory (RDT) (Batchelor & Proudman 1954; Hunt 1973), and provided a better agreement with the experimental measurements. Many of the analytical solutions for airfoils in non-uniform flows were based on the theoretical framework developed by Goldstein & Atassi (1976) and Goldstein (1978), in which the velocity field is split into a rotational part that corresponds to the vortical disturbance and an irrotational part that is linked to the acoustic component. Owing to the non-uniform mean flow, the turbulence statistics would be changed during the distortion of the incoming gusts, and the properties of sound generation are altered (Christophe, Anthoine & Moreau 2009; Christophe 2011). A method to account for this effect is to employ the modified turbulence spectra based on the RDT as inputs of the Amiet solution (Santana *et al.* 2016; Miotto, Wolf & de Santana 2017, 2018).

For the acoustic responses by real airfoils, Kerschen & Balsa (1981), Kerschen & Myers (1987), Tsai (1992) and Myers & Kerschen (1997) conducted a series of analytical solutions based on Goldstein's decomposition. However, the methods suffer from the singularity issue at the stagnation point because of the appearance of zero mean flow velocity in the denominator of the 'drift function' (Lighthill 1956). To solve the singularity issue, Ayton & Peake (2015, 2016), Ayton (2016) and Ayton & Chaitanya (2017) introduced new asymptotic regions, and improved the predictions of leading-edge noise. Another method to remove the singularity was developed by Atassi & Grzedzinski (1989) by introducing an additional decomposition of

the velocity field to Goldstein's method. Then, an inhomogeneous convected wave equation with spatially varying coefficients was solved numerically (Scott & Atassi 1990; Atassi, Dusey & Davis 1993*a*; Atassi, Fang & Patrick 1993*b*) with alternative source terms and mixed boundary conditions on the airfoil surface (hard wall), in the flow wake region (the Kutta condition) and in the acoustic far field (related to the gust distortion). Another method (without using RDT) was based on the unsteady vortex-based panel method (Glegg & Devenport 2010), which improved the prediction accuracy with refined panels (Devenport *et al.* 2010). Other investigations based on the panel method can be found in Lysak (2011) and Santana, Schram & Desmet (2012). The development of those theoretical analyses played an important role in enhancing our understanding of the problem of leading-edge noise. However, the associated models become progressively more complicated and convoluted than Amiet's initial flat-plate solution.

In this work, we revisit the problem of leading-edge noise (also called gust–airfoil interaction noise) in a non-uniform mean flow, and attempt to develop a correction to Amiet's solution for more realistic applications. For the flat-plate configuration, the governing equation for the unsteady fluctuations is the convected wave equation, which can be simplified to a classical wave equation by the Prandtl–Glauert transformation (Rienstra & Hirschberg 2004). The Schwarzschild technique or Wiener–Hopf method is then applied to solve the equation with mixed boundary conditions. For cases with real airfoil geometry, the difficulty in solving the equation is due to the complexity of the governing equation with spatially dependent coefficients. One main contribution of the current work is the introduction of a new space–time transformation, by which the governing equation for the unsteady fluctuations is approximated as a classical wave equation in the transformed domain. The transformation is analogous to the Prandtl–Glauert transformation, but allows for non-uniform coefficients by the local mean flows. The boundary conditions in the regions ahead of the airfoil, on the airfoil and in the wake are similar to those previously applied in the flat-plate solution (Amiet 1976*a*), and the Schwarzschild technique is then employed to obtain the solution. Compared with the previous analytical studies (Christophe *et al.* 2009; Santana *et al.* 2016; Miotto *et al.* 2017), the proposed correction method does not consider the variation of the turbulence statistics due to a realistic airfoil configuration. Analysis of the singularity property at the stagnation point like that by Ayton & Peake (2016) and Ayton & Chaitanya (2017) is not conducted either. The performance of the correction depends on (1) the error induced by the space–time transformation, and (2) the validity of employing the same boundary conditions as the flat-plate solution. The implications are discussed in this work by comparison with high-order CAA results. In general, the prediction of the airfoil leading-edge noise using the proposed method is more accurate for lower-frequency gusts at lower flow speeds since the approximation error increases with frequency and Mach number. Nevertheless, it improves the prediction accuracy of the flat-plate solution, which does not consider the effect of real airfoil geometry.

The remaining parts of the paper are organised as follows. Section 2 derives the formulations of the proposed correction to the flat-plate solution. Section 3 applies the method to several representative airfoils at varies Mach numbers. Both single-frequency and broadband cases are considered. Section 4 is a summary.

## 2. Formulation

Figure 1 shows a schematic for the sound generated by the interaction of a gust and a real airfoil, in which the streamline across the stagnation point deviates from

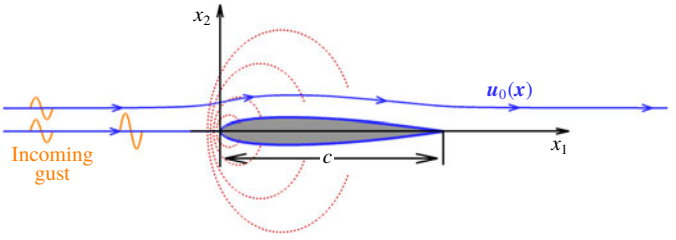


FIGURE 1. Schematic of the airfoil leading-edge noise in non-uniform flow.

the $x_1$-axis, and the mean flow non-uniformity may eventually affect the leading-edge noise. The chord length is $c$, the non-uniform mean flow is denoted by $\boldsymbol{u}_0(\boldsymbol{x})$, and the governing equation in the non-uniform mean flow is (Goldstein 1978)

$$\frac{\mathrm{D}_0}{\mathrm{D}t}\left(\frac{1}{a_0^2}\frac{\mathrm{D}_0\phi}{\mathrm{D}t}\right)-\frac{1}{\rho_0}\nabla\cdot(\rho_0\nabla\phi)=\frac{1}{\rho_0}\nabla\cdot(\rho_0\boldsymbol{v}_g'). \tag{2.1}$$

Here $\phi$ is the velocity potential of the induced fluctuation field, $\mathrm{D}_0/\mathrm{D}t=\partial/\partial t+\boldsymbol{u}_0\cdot\nabla$ is the material derivative of the non-uniform mean flow, $a_0$ is the local speed of sound, $\rho_0$ is the local density and $\boldsymbol{v}_g'$ is the velocity fluctuation of the incoming gust. In addition, the relationship between the induced unsteady pressure $p$ and the velocity potential $\phi$ is obtained from the unsteady Bernoulli equation (Batchelor 1967)

$$p(\boldsymbol{x},t)=-\rho_0\frac{\mathrm{D}_0\phi}{\mathrm{D}t}=-\rho_0\left(\frac{\partial}{\partial t}+\boldsymbol{u}_0\cdot\nabla\right)\phi(\boldsymbol{x},t). \tag{2.2}$$

The same boundary conditions as adopted by Amiet (1976*a*) for the flat-plate solution are employed. In the regions ahead of the airfoil and in the wake region, the induced velocity potential (of the acoustic wave by the incoming gust distortion) are specified as

$$\phi(x_1,0)=0,\quad \text{for } x_1<0;\qquad \frac{\mathrm{D}_0}{\mathrm{D}t}\phi(x_1,0)=0,\quad \text{for } x_1>c. \tag{2.3a,b}$$

On the airfoil surface, the hard-wall condition leads to the following boundary condition:

$$\boldsymbol{n}\cdot(\nabla\phi+\boldsymbol{v}_g')=0\quad\Rightarrow\quad\frac{\partial\phi}{\partial n}=w(\boldsymbol{x},t)\triangleq-\boldsymbol{n}\cdot\boldsymbol{v}_g'. \tag{2.4}$$

### 2.1. *Remarks on the boundary conditions for practical applications*

In this work, the velocity of the incoming gust is assumed to be the same as in the far field, i.e. the following representation of the gust in the theoretical application is used:

$$\boldsymbol{v}_g'(\boldsymbol{x},t)=(u_g',v_g')=(-k_2,k_1)\frac{A_v}{\sqrt{k_1^2+k_2^2}}\exp(\mathrm{i}\omega t-\mathrm{i}k_1x_1-\mathrm{i}k_2x_2),\qquad \omega=k_1u_\infty. \tag{2.5}$$

However, in practical situations, the gust experiences distortion by the non-uniform mean flow; the value of $\boldsymbol{v}_g'$ should gradually differ from (2.5). One consequence of the gust distortion is that the turbulence statistics (for the broadband case) might be altered, as has been studied in the previous works by Moreau *et al.* (2005),

Christophe *et al.* (2009), Christophe (2011) and Santana *et al.* (2016). In this case, one possible approach to account for this effect is to use the theory by Goldstein (1978) that considers the distortion of the gusts. Atassi & Grzedzinski (1989) modified Goldstein's formulation to remove the singularity, and the method was employed by Scott & Atassi (1990) for numerical calculation. However, the problem in using the modified method is that the boundary condition ahead of the airfoil ($\phi = 0$ when $x_1 < 0$) is not given, making it difficult to solve the equation analytically. Any numerical approach to solve (2.1) should be conducted in the 2-D domain. Therefore, the analytical study proposed in this work should be viewed as a correction method to the flat-plate solution rather than an exact solution for real airfoils.

### 2.2. *Analytical solution*

#### 2.2.1. *Sound governing equation in the transformed coordinates*

To account for the effect of background mean flow on the acoustic process, a coordinate transformation is introduced in the general form

$$X_1 = F(x_1), \quad X_2 = G(x_2), \quad T = \eta t + \Psi(x_1, x_2). \tag{2.6a–c}$$

The following relationships can be obtained:

$$\frac{\partial}{\partial x_1} = f(x_1)\frac{\partial}{\partial X_1} + \Psi_1\frac{\partial}{\partial T}, \quad \frac{\partial}{\partial x_2} = g(x_2)\frac{\partial}{\partial X_2} + \Psi_2\frac{\partial}{\partial T}, \quad \frac{\partial}{\partial t} = \eta\frac{\partial}{\partial T}, \tag{2.7a–c}$$

where $f(x_1) = F'(x_1)$, $g(x_2) = G'(x_2)$, $\Psi_1 = \partial\Psi/\partial x_1$ and $\Psi_2 = \partial\Psi/\partial x_2$. When the background mean flow is uniform, the governing equation is the convected wave equation, which can be reduced to a classical wave equation by using the Prandtl–Glauert transformation: $X_1 = x_1/\beta_\infty$, $X_2 = x_2$ and $T = \beta_\infty t + M_\infty x_1/(a_\infty\beta_\infty)$. In this case $f = 1/\beta_\infty$, $g = 1$, $\eta = \beta_\infty$, $\partial\Psi/\partial x_1 = M_\infty/(a_\infty\beta_\infty)$ and $\partial\Psi/\partial x_2 = 0$. The factor $\beta_\infty$ is introduced to account for the convection effect by the streamwise uniform mean flow. However, large errors exist in practical applications with non-uniform mean flow, which motivates this work. To tackle the problem, we develop a generalised space–time transformation that is analogous to the Prandtl–Glauert transformation. The coefficients in the space–time transformation are determined by the local flow variables

$$X_1 = \int_{\mathcal{L}} \frac{\mathrm{d}\xi_1}{\beta_1(\boldsymbol{\xi})}, \quad X_2 = \int_{\mathcal{L}} \frac{\mathrm{d}\xi_2}{\beta_2(\boldsymbol{\xi})}, \quad T = \beta_\infty t + \Psi. \tag{2.8a–c}$$

Here the notation $(\cdot)_{\mathcal{L}}$ means that the integrations are performed along the streamline $\mathcal{L}$ from $\boldsymbol{\xi} = \mathbf{0}$ to $\boldsymbol{\xi} = (x_1, x_2)$, $\beta_1 = \sqrt{1 - M_1^2}$, $\beta_2 = \sqrt{1 - M_2^2}$, $M_1(\boldsymbol{x}) = u_1(\boldsymbol{x})/a_0(\boldsymbol{x})$ and $M_2(\boldsymbol{x}) = u_2(\boldsymbol{x})/a_0(\boldsymbol{x})$ are the local Mach numbers, and

$$\frac{\partial\Psi}{\partial x_1} = \frac{M_1}{\beta_1 a_0}, \quad \frac{\partial\Psi}{\partial x_2} = \frac{M_2}{\beta_2 a_0} \quad \Rightarrow \quad \Psi(x_1, x_2) = \int_{\mathcal{L}} \left[\frac{\partial\Psi}{\partial\xi_1}\mathrm{d}\xi_1 + \frac{\partial\Psi}{\partial\xi_2}\mathrm{d}\xi_2\right]. \tag{2.9a,b}$$

One can then obtain that

$$f(\boldsymbol{x}) = \frac{1}{\beta_1(\boldsymbol{x})}, \quad g(\boldsymbol{x}) = \frac{1}{\beta_2(\boldsymbol{x})}, \quad \eta = \beta_\infty. \tag{2.10a–c}$$

Equations (2.8) can be viewed as a generalisation of the Prandtl–Glauert transformation where the coefficients $\beta_\infty$ and $M_\infty$ are replaced by the non-uniform ones $\beta_1$, $\beta_2$,

$M_1$ and $M_2$. An integration along the streamline is used to account for the dependence of the new coordinate variables $\boldsymbol{X}$ on the original one $\boldsymbol{x}$. With the new transformation, the following classical wave equation is solved in the transformed domain:

$$\frac{\partial^2\phi}{\partial T^2} - a_0^2\left(\frac{\partial^2\phi}{\partial X_1^2} + \frac{\partial^2\phi}{\partial X_2^2}\right) = \mathscr{E}. \tag{2.11}$$

To obtain the solution, usually we need to omit $\mathscr{E}$, which is the approximation error due to the space–time transformation. The dependence of $\mathscr{E}$ on the flow speed is analysed in appendix A. In general, the magnitude of the errors for most terms are $O(M_\infty^2)$ or $O(M_\infty^3)$, while the error of the time derivative $\partial\phi/\partial T$ is $O(M_\infty)$, suggesting that there could be larger errors at higher frequencies at higher Mach numbers. In the theoretical analysis, we can assume that the variables are time harmonic such that

$$\phi(\boldsymbol{x}, t) = \hat{\phi}(\boldsymbol{x})\mathrm{e}^{\mathrm{i}\omega t} = \hat{\phi}(\boldsymbol{x})\exp\left[\frac{\mathrm{i}\omega(T-\Psi)}{\eta}\right] = \varphi(\boldsymbol{X})\mathrm{e}^{\mathrm{i}\Omega T}, \tag{2.12}$$

where $\omega$ is the angular frequency in the original space, while $\Omega = \omega/\eta$ is the angular frequency in the transformed domain, i.e. the variables have a time dependence $\mathrm{e}^{\mathrm{i}\Omega T}$ and the amplitudes in the two domains are related by

$$\varphi(\boldsymbol{X}) = \hat{\phi}(\boldsymbol{x})\mathrm{e}^{-\mathrm{i}\Omega\Psi}. \tag{2.13}$$

The same relation is also applicable for other variables. Now we consider representations of the boundary conditions in the transformed domain. In the region ahead of the airfoil, it is straightforward to obtain that

$$\varphi(X_1, 0) = 0, \quad \text{for } X_1 < 0. \tag{2.14}$$

Similarly, the boundary condition in the wake region is written as

$$\tilde{p}(\boldsymbol{X}) = 0, \quad \text{for } X_1 > C, \tag{2.15}$$

where $\tilde{p}$ is the spatial part of the sound pressure written in the transformed domain. On the airfoil surface $0 \leqslant X_1 \leqslant C$, the hard-wall condition (2.4) is

$$\begin{aligned} w = n_1\frac{\partial\phi}{\partial x_1} + n_2\frac{\partial\phi}{\partial x_2} &= \left(n_1\frac{\partial\Psi}{\partial x_1} + n_2\frac{\partial\Psi}{\partial x_2}\right)\frac{\partial\phi}{\partial T} + n_1 f\frac{\partial\phi}{\partial X_1} + n_2 g\frac{\partial\phi}{\partial X_2}, \\ \Rightarrow \quad \frac{\partial\phi}{\partial X_2} &= \frac{1}{n_2 g}\left[w - \left(n_1\frac{\partial\Psi}{\partial x_1} + n_2\frac{\partial\Psi}{\partial x_2}\right)\frac{\partial\phi}{\partial T} - n_1 f\frac{\partial\phi}{\partial X_1}\right]. \end{aligned} \tag{2.16}$$

With the time-dependent term $\mathrm{e}^{\mathrm{i}\Omega T}$ omitted, the condition can be represented as

$$\frac{\partial\varphi}{\partial X_2} = \tilde{W}(\boldsymbol{x}) \triangleq \frac{1}{n_2 g}\left[W - \mathrm{i}\Omega\left(n_1\frac{\partial\Psi}{\partial x_1} + n_2\frac{\partial\Psi}{\partial x_2}\right)\varphi - n_1 f\frac{\partial\varphi}{\partial X_1}\right], \quad \text{for } 0 \leqslant X_1 \leqslant C, \tag{2.17}$$

where $W(\boldsymbol{X}) = \hat{w}(\boldsymbol{x})\exp(-\mathrm{i}\Omega\Psi)$ and $\hat{w}$ is the spatially dependent part of $w(\boldsymbol{x}, t)$ defined in (2.4), i.e. $w(\boldsymbol{x}, t) = W(\boldsymbol{X})\mathrm{e}^{\mathrm{i}\Omega T}$.

In summary, with the term $\mathscr{E}$ omitted, the equivalent Helmholtz equation to solve in the new coordinates is

$$\mathcal{K}^2\varphi + \left(\frac{\partial^2\varphi}{\partial X_1^2} + \frac{\partial^2\varphi}{\partial X_2^2}\right) = 0, \quad \mathcal{K} = \frac{\Omega}{a_\infty}, \tag{2.18}$$

where $\Omega = \omega/\beta$, and $\varphi$ is the spatially varying part of the velocity potential in the transformed domain, which is defined in (2.12) and (2.13). The boundary conditions in different regions of the streamline $\mathcal{L}$ are

$$\left.\begin{array}{rl} \varphi(\boldsymbol{X}) = 0, & X_1 < 0, \\ \dfrac{\partial \varphi(\boldsymbol{X})}{\partial X_2} = \tilde{W}(\boldsymbol{X}), & 0 \leqslant X_1 \leqslant C, \\ \tilde{p}(\boldsymbol{X}) = 0, & X_1 > C. \end{array}\right\} \tag{2.19}$$

Having obtained the (approximate) classical wave equation, which is the main contribution of this paper, the Schwarzschild technique (Schwarzschild 1901) is used to obtain the solution of pressure fluctuation on the airfoil surface. The procedures are similar to that given in Amiet (1976*a*), but with some slight modifications due to the non-uniformities of the mean flow variables. The details are provided in the next section for completeness. When the pressure fluctuation on the airfoil surface is computed, the Kirchhoff–Helmholtz integral, which is equivalent to Curle's acoustic analogy (Curle 1955; Christophe 2011) for this problem, is applied to compute the sound distribution at the given observers (that are often in the far field).

In the solution, we need to compute the relationship between the pressure fluctuation $p(\boldsymbol{x}, t)$ and velocity potential $\phi(\boldsymbol{x}, t)$ in the transformed domain. From (2.2) and (2.7), the two variables are related by

$$-\frac{p}{\rho_0} = \frac{\mathrm{D}_0\phi}{\mathrm{D}t} = \left[\left(\eta + u_1\frac{\partial \Psi}{\partial x_1} + u_2\frac{\partial \Psi}{\partial x_2}\right)\frac{\partial}{\partial T} + u_1 f\frac{\partial}{\partial X_1} + u_2 g\frac{\partial}{\partial X_2}\right]\phi. \tag{2.20}$$

The difficulty in using this equation is that the value of $\partial\phi/\partial X_2$ may depend on the transverse coordinate $X_2$, while all integration and differential calculations are performed along the streamline in the analytical derivations. Therefore, we need to replace this term with functions that depend only on $X_1$. For simplicity, equation (2.20) is denoted as

$$\tilde{p} = -\rho_0\left[\left(\mathrm{i}\Omega\Gamma + \Theta\frac{\partial}{\partial X_1}\right)\varphi + \mathscr{T}\right]. \tag{2.21}$$

In the regions ahead of the airfoil leading edge and after the airfoil trailing edge, we assume that $\partial\phi/\partial X_2$ is small such that

$$\Gamma = \eta + u_1\frac{\partial \Psi}{\partial x_1} + u_2\frac{\partial \Psi}{\partial x_2}, \quad \Theta = u_1 f, \quad \mathscr{T} = 0, \quad \text{for } X_1 < 0 \text{ or } X_1 > C. \tag{2.22a–c}$$

On the airfoil surface ($0 \leqslant X_1 \leqslant C$), a combination of (2.17) and (2.20) yields

$$\Gamma = \eta + u_1\frac{\partial \Psi}{\partial x_1} + u_2\frac{\partial \Psi}{\partial x_2} - \frac{u_2}{n_2}\left(n_1\frac{\partial \Psi}{\partial x_1} + n_2\frac{\partial \Psi}{\partial x_2}\right) = \eta + \left(\frac{u_1 n_2 - u_2 n_1}{n_2}\right)\frac{\partial \Psi}{\partial x_1}. \tag{2.23}$$

By introducing a new variable $V = u_1 n_2 - u_2 n_1$, which is the flow velocity along the streamline, we can compute $\Gamma$, $\Theta$ and $\mathscr{T}$ as

$$\Gamma = \eta + \frac{V}{n_2}\frac{\partial \Psi}{\partial x_1}, \quad \Theta = \frac{f V}{n_2}, \quad \mathscr{T} = \frac{\tilde{W} u_2}{n_2}, \quad \text{for } 0 \leqslant X_1 \leqslant C. \tag{2.24a–c}$$

Equation (2.21) suggests that the sound pressure $\tilde{p}$ (or $p$ in the original domain) can be computed from the known value of $\varphi(\boldsymbol{X})$. Conversely, $\varphi$ can also be solved from the known value of $\tilde{p}$ based on the ordinary differential equation (ODE)

$$\frac{\partial \varphi}{\partial X_1} + a(X_1)\varphi = b(X_1), \tag{2.25}$$

where the coefficients are determined from (2.21):

$$a(X_1) = \frac{\mathrm{i}\Omega\Gamma}{\Theta}, \quad b(X_1) = -\frac{1}{\Theta}\left(\frac{\tilde{p}}{\rho_0} + \mathscr{T}\right). \tag{2.26a,b}$$

Then the solution to this ODE is (cf. section 2.4 in Goodwine (2010)):

$$\varphi(X_1) = \frac{\mathcal{F}_1(X_1)}{\mathcal{F}_2(X_1)}, \quad \text{where} \quad \left.\begin{aligned} \mathcal{F}_1(X_1) &= \int_{-\infty}^{X_1} b(\xi)\exp\left(\int_{-\infty}^{\xi} a(\eta)\,\mathrm{d}\eta\right)\mathrm{d}\xi, \\ \mathcal{F}_2(X_2) &= \exp\left(\int_{-\infty}^{X_1} a(\xi)\,\mathrm{d}\xi\right). \end{aligned}\right\} \tag{2.27}$$

2.2.2. *Solution using the Schwarzschild technique*

The Schwarzschild solution is used to compute the pressure fluctuation on the airfoil surface, which will then be used for the computation of the sound pressure at the observer points elsewhere. Usually, the Schwarzschild solution is valid for the Helmholtz equation with two-section semi-infinite mixed boundary conditions (Schwarzschild 1901; Amiet 1976*a*)

$$\nabla_X^2\varphi + \mathcal{K}^2\varphi = 0, \quad \varphi(X_1, 0) = F(X_1), \quad \text{for } X_1 \geqslant 0; \quad \frac{\partial\varphi}{\partial X_2} = 0, \quad \text{for } X_1 < 0. \tag{2.28a,b}$$

Then the solution for any $X_1 < 0$ is

$$\varphi(X_1, 0) = \frac{1}{\pi}\int_0^{\infty}\sqrt{\frac{-X_1}{\xi}}\frac{\mathrm{e}^{-\mathrm{i}\mathcal{K}(\xi - X_1)}}{\xi - X_1}F(\xi)\,\mathrm{d}\xi. \tag{2.29}$$

The equation studied in this work, however, has three-section mixed boundary conditions in the regions $X_1 < 0$, $0 \leqslant X_1 \leqslant C$ and $X_1 > C$, respectively. In this work, we will follow the procedures proposed by Amiet (1976*a*) to treat every two adjacent sections as semi-infinite to meet the requirement of the Schwarzschild solution. Then, leading-edge and trailing-edge corrections are introduced to meet the overall boundary conditions illustrated in (2.19).

Firstly, a zeroth-order solution is constructed that satisfies the hard-wall condition $\partial\varphi/\partial X_2 = \tilde{W}$. However, the value of $\varphi$ (see (2.17)) is unknown at the beginning of the computation. The strategy adopted in this work is to use an iterative approach by initially letting $\tilde{W} = W/n_2 g$, and then compute the zeroth-order solution by the Green's function method, following the standard technique (Amiet 1976*a*):

$$\varphi^{(0)}(X_1, X_2) = \frac{\mathrm{i}}{4}\int_{\mathcal{L}}\tilde{W}(\xi)H_0^{(2)}\left(\mathcal{K}\sqrt{(X_1 - \xi)^2 + (X_2 - \eta(\xi))^2}\right)\mathrm{d}\xi. \tag{2.30}$$

Letting $\varphi = \varphi^{(0)}$ given in (2.17), we can get an updated value of $\tilde{W}$. This procedure is repeated until the solution of (2.30) is convergent. Then the solution for $\varphi = \varphi^{(0)}$ can be obtained that satisfies the hard-wall condition $\partial\varphi^{(0)}/\partial X_2 = \tilde{W}$ for all $X_1 \in \mathbb{R}$. However, in practical situations, alternative boundary conditions should be applied in the regions before and after the airfoil, i.e. $X_1 < 0$ or $X_1 > C$. The key measure in the analytical derivation is to find a corrected solution $\psi^{(0)}$ that satisfies

$$\psi^{(0)}(X_1, 0) = -\varphi^{(0)}(X_1, 0), \quad \text{for } X_1 < 0; \quad \text{and} \quad \frac{\partial \psi^{(0)}(X_1, 0)}{\partial X_2} = 0, \quad \text{for } X_1 \geqslant 0. \tag{2.31a,b}$$

As a result, the corrected solution $\varphi^{(1)} = \varphi^{(0)} + \psi^{(0)}$ satisfies the mixed boundary condition that $\varphi^{(1)} = 0$ for $X_1 < 0$ and $\partial\varphi^{(1)}/\partial X_2 = W$ for $X_1 \geqslant 0$. The solution of $\psi^{(0)}$ to (2.31) can be solved using the Schwarzschild technique. For simplicity, the notation $\mathcal{X}_1 = -X_1$ and $\mathcal{X}_2 = X_2$ is introduced, and the boundary conditions for $\psi^{(0)}$ are

$$\psi^{(0)}(\mathcal{X}_1, 0) = -\varphi^{(0)}(-\mathcal{X}_1, 0), \quad \text{for } \mathcal{X}_1 \geqslant 0; \quad \text{and} \quad \frac{\partial \psi^{(0)}(\mathcal{X}_1, 0)}{\partial \mathcal{X}_2} = 0, \quad \text{for } \mathcal{X}_1 < 0. \tag{2.32a,b}$$

Then for any $\mathcal{X}_1 = -X_1 < 0$, the Schwarzschild solution yields

$$\psi^{(0)}(\mathcal{X}_1, 0) = -\frac{1}{\pi}\int_0^\infty \sqrt{\frac{-\mathcal{X}_1}{\xi}}\frac{\mathrm{e}^{-\mathrm{i}\mathcal{K}(\xi - \mathcal{X}_1)}}{\xi - \mathcal{X}_1}\varphi^{(0)}(-\xi, 0)\,\mathrm{d}\xi, \quad \forall\ \mathcal{X}_1 < 0. \tag{2.33}$$

It can then be equivalently written in the $(X_1, X_2)$ coordinates as

$$\psi^{(0)}(X_1, 0) = -\frac{1}{\pi}\int_0^\infty \sqrt{\frac{X_1}{\xi}}\frac{\mathrm{e}^{-\mathrm{i}\mathcal{K}(\xi + X_1)}}{\xi + X_1}\varphi^{(0)}(-\xi, 0)\,\mathrm{d}\xi, \quad \forall\ X_1 > 0. \tag{2.34}$$

Then, the induced sound pressure $\tilde{p}^{(1)}$ can be computed from $\varphi^{(1)} = \varphi^{(0)} + \psi^{(0)}$ based on (2.21):

$$\tilde{p}^{(1)}(\xi) = -\rho_0\left[\left(\mathrm{i}\Omega\Gamma + \Theta\frac{\partial}{\partial X_1}\right)\varphi^{(1)} + \mathscr{T}\right]. \tag{2.35}$$

Physically, the hard-wall condition (which is utilised to get $\psi^{(0)}$ and $\tilde{p}^{(1)}$) suggests that $\partial\tilde{p}^{(1)}/\partial X_2 \approx 0$ in the region $X_1 \geqslant 0$, which conflicts with the zero-pressure condition in the wake region ($X_1 \geqslant C$). To address this point, the next step in the proposed method is to introduce a pressure correction $q^{(1)}$ that cancels $\tilde{p}^{(1)}$ in the wake region while it satisfies the hard-wall condition on the airfoil surface:

$$q^{(1)}(X_1, 0) = -\tilde{p}^{(1)}(X_1, 0), \quad \text{for } X_1 > C; \quad \frac{\partial q^{(1)}}{\partial X_2}(X_1, 0) = 0, \quad \text{for } X_1 \leqslant C. \tag{2.36a,b}$$

Again, the notation $\mathscr{X}_1 = X_1 - C$ is defined to simplify the boundary conditions:

$$q^{(1)}(\mathscr{X}_1, 0) = -\tilde{p}^{(1)}(\mathscr{X}_1 + C, 0), \quad \text{for } \mathscr{X}_1 \geqslant 0; \quad \text{and} \quad \frac{\partial q^{(1)}}{\partial \mathscr{X}_2}(\mathscr{X}_1, 0) = 0, \quad \text{for } \mathscr{X}_1 \leqslant 0. \tag{2.37a,b}$$

Then the Schwarzschild solution is obtained as

$$q^{(1)}(\mathscr{X}_1, 0) = -\frac{1}{\pi}\int_0^\infty \sqrt{\frac{-\mathscr{X}_1}{\xi}}\frac{\mathrm{e}^{-\mathrm{i}\mathcal{K}(\xi-\mathscr{X}_1)}}{\xi-\mathscr{X}_1}\tilde{p}^{(1)}(\xi+C, 0)\,\mathrm{d}\xi, \tag{2.38}$$

which could be equivalently written as

$$q^{(1)}(X_1, 0) = -\frac{1}{\pi}\int_0^\infty \sqrt{\frac{r}{\xi}}\frac{\mathrm{e}^{-\mathrm{i}\mathcal{K}(\xi+r)}}{\xi+r}\tilde{p}^{(1)}(\xi+C, 0)\,\mathrm{d}\xi, \quad r = C - X_1. \tag{2.39}$$

The second-order approximation of the pressure field $\tilde{p}^{(2)} = \tilde{p}^{(1)} + q^{(1)}$ satisfies $\tilde{p}^{(2)}(X_1) = 0$ for $X_1 \geqslant C$ (in the wake region) and $\partial p^{(2)}/\partial X_2 = 0$ for $X_1 < C$ (ahead of and on the airfoil). However, it is possible that the corresponding velocity potential $\varphi^{(2)} \neq 0$ in the region $X_1 < 0$. By assumption, this mismatch can be reduced by repeating the correction procedures that iteratively assign $\varphi^{(2)}$ to $\varphi^{(0)}$ until the solution converges (Amiet 1976*a*). To repeat these procedures, we need to compute $\varphi$ from the known distribution of $\tilde{p}^{(2)}$ based on (2.27). The final output of the Schwarzschild solution is the sound pressure $\tilde{p}(\boldsymbol{x}) = \tilde{p}^{(2)}(\boldsymbol{x})$ on the airfoil surface.

### 2.2.3. *Sound pressure in the far field*

We use the Kirchhoff–Helmholtz integral (identical to the Curle (1955) integral for this problem) to compute the sound at the far-field observers after the convergent solution (of $\tilde{p}(\boldsymbol{x}) = \tilde{p}^{(2)}(\boldsymbol{x})$ on the airfoil surface) is obtained. To avoid misunderstanding, the coordinates at the local point are denoted as $(Y_1, Y_2)$ and the coordinates at the observer point are $(X_1, X_2)$, and the Green's function is denoted as $G(X_1, X_2; Y_1, Y_2)$ in the transformed domain (by using (2.6)). The following equations are obtained:

$$G(\mathcal{K}^2 + \nabla^2)\tilde{p} = 0, \quad \tilde{p}(\mathcal{K}^2 + \nabla^2)G = \tilde{p}\delta(\boldsymbol{X} - \boldsymbol{Y}). \tag{2.40a,b}$$

The pressure distribution at the observer point $(X_1, X_2)$ is obtained as

$$\tilde{p}(X_1, X_2) = \int_V (\tilde{p}\nabla^2 G - G\nabla^2\tilde{p})\,\mathrm{d}\boldsymbol{Y} = \int_V \boldsymbol{\nabla}\cdot(\tilde{p}\boldsymbol{\nabla}G - G\boldsymbol{\nabla}\tilde{p})\,\mathrm{d}\boldsymbol{Y}. \tag{2.41}$$

The integral can be simplified and performed only on the airfoil surface based on the Gaussian theorem. From the hard-wall condition, the integral is reduced to

$$\tilde{p}(\boldsymbol{X}) = \int_{\mathcal{L}} \tilde{p}(Y_1)\frac{\partial G}{\partial X_2}\,\mathrm{d}l, \tag{2.42}$$

where $\mathcal{L}$ is the section of the streamline on the airfoil surface, and the Green's function of the Helmholtz equation in the 2-D domain is (Crighton 1975)

$$G(X_1, X_2; Y_1, Y_2) = \frac{\mathrm{i}}{4}H_0^{(2)}\left(\mathcal{K}\sqrt{(X_1 - Y_1)^2 + (X_2 - Y_2)^2}\right). \tag{2.43}$$

Once the equation is solved (in the $\boldsymbol{X}$–$T$ domain), we need to compute the variables in the original coordinate. In the far field, the flow is nearly uniform such that $\beta_1 \to \beta_\infty$, $\beta_2 \to 1$ and $u \to u_\infty$. The time–space transformation at the observer points is

$$X_1 = \frac{x_1}{\beta_\infty}, \quad X_2 = x_2. \tag{2.44a,b}$$

In addition, the sound pressure $p(\boldsymbol{x}, t)$ in the original domain is related to the computed value $\tilde{p}(\boldsymbol{X})$ in the transformed domain by

$$p(\boldsymbol{x})\mathrm{e}^{\mathrm{i}\omega t} = p(\boldsymbol{x})\mathrm{e}^{-\mathrm{i}\Omega\Psi_\infty}\mathrm{e}^{\mathrm{i}\Omega T} = \tilde{p}(X_1, X_2)\mathrm{e}^{\mathrm{i}\Omega T} \quad \Rightarrow \quad p(\boldsymbol{x}) = \tilde{p}(\boldsymbol{X})\mathrm{e}^{\mathrm{i}\Omega\Psi_\infty}, \tag{2.45}$$

where $\Psi_\infty = M_\infty x_1/(\beta_\infty a_\infty)$, since the flow around the observers is uniform.

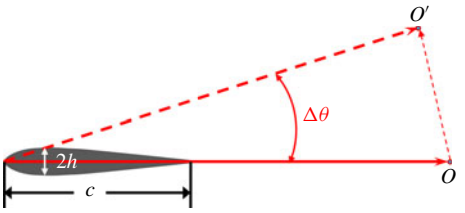


FIGURE 2. Schematic of observer angle correction for real airfoil geometry.

2.2.4. *Semi-empirical corrections of the observer angles*

In previous numerical studies of leading-edge noise, it was found that the angles of the radiation lobes tend to be at higher observer angles for airfoils with finite thickness (Gill *et al.* 2013). In this work, a semi-empirical correction formulation is developed under the assumption that the shift of radiation angles is caused by the shielding effect of the airfoil. As illustrated in figure 2, the sound that is expected to propagate to observer point $O$ might go to $O'$ due to the airfoil geometry. However, this effect is not considered in the proposed analytical model. To account for the effect, an angle $\Delta\theta$ is introduced,

$$\Delta\theta \approx \tan\Delta\theta = \frac{h}{c}, \tag{2.46}$$

where $h$ is a half of the airfoil thickness. Then, a transformation for the observer angle correction is employed:

$$\theta^* = \Delta\theta + \frac{\pi - \Delta\theta}{\pi}\theta, \quad \text{for } \theta \in (0, \pi). \tag{2.47}$$

This means that the downstream observer angle $\theta = 0$ is transformed to $\Delta\theta$ while the upstream observer angle $\theta = \pi$ remains unchanged. One drawback of this correction is that, in the region $\theta \in (0, \Delta\theta)$, there is a shadow region and no data are available.

### 2.3. *Summary of the correction method*

The proposed analytical correction in general follows the procedures in Amiet's (1976*a*) flat-plate solution, while the flow non-uniformity in the near field is considered. The generalised spatio-temporal transformation in (2.8) only requires the mean flow distribution along the streamline across the stagnation point. It is therefore applicable for applications with non-uniform far upstream conditions. Representations of the approximation error in appendix A should be similar, but the magnitude of each term could be different. However, the sound propagation and radiation might be changed due to the non-uniformity, and the validity of the Schwarzschild technique is called into question. Also, the gust could experience distortion from far upstream, and the effect on the sound property of the locations that introduce the gust is a variable to be investigated. In addition, to introduce gust or synthetic turbulence in the computational domain without causing spurious wave generation in the non-uniform mean flow is still challenging for CAA, and the validation or verification of the theoretical correction method could thus be difficult. Therefore, we adopt the simplifications and assumptions of uniform far upstream conditions as in most of the previous leading-edge noise studies (Amiet 1975; Myers & Kerschen 1997; Ayton 2016). For practical applications, the key steps in the method are summarised as follows:

(i) Compute themean flow variables along the streamline that crosses the stagnation point.
(ii) Compute $w(\boldsymbol{x}, t)$ by (2.4) for the given oncoming vortical gust.
(iii) Compute the coordinate variables $\boldsymbol{X}$, $T$ and the relevant variables $\Omega$, $\mathcal{K}$, etc.
(iv) Compute the zeroth-order solution $\varphi^{(0)}$ by (2.30), using the value of $w(\boldsymbol{x}, t)$.
(v) Compute the leading-edge correction by (2.34), then let $\psi^{(1)} = \varphi^{(0)} + \psi^{(0)}$.
(vi) Compute the sound pressure $\tilde{p}^{(1)}$ by (2.21) based on $\psi^{(1)}$.
(vii) Compute the trailing-edge correction by (2.39), then let $\tilde{p}^{(2)} = \tilde{p}^{(1)} + q^{(1)}$.
(viii) Compute $\varphi^{(2)}$ by (2.27) based on $\tilde{p}^{(2)}$ on the streamlines.
(ix) Let $\varphi^{(0)} = \varphi^{(2)}$ and repeat steps (v)–(viii) till the solution is convergent.
(x) Compute the sound pressure $\tilde{p}(\boldsymbol{X})$ at the observers from (2.42).
(xi) Compute $p(\boldsymbol{x})$ from (2.45), and apply the angle correction.

## 3. Results and discussion

In this section, we will apply the analytical correction to the NACA four-digit airfoils with different thickness (ranges from 2 % to 18 %). In this method, the non-uniform distributions of $u_1(\boldsymbol{x})$, $u_2(\boldsymbol{x})$ and $a_0(\boldsymbol{x})$ along the streamlines across the stagnation point are needed. For simplicity, the variables are computed using the panel method based on the potential flow theory (Drela 1989). In practical application, the variables can also be obtained from the simulations of the flow governing equations, which, however, are more expensive that the panel method employed in this work. Also, the background mean flow variables could be assumed to be uniform such that the solution is reduced to Amiet's result. The effects of airfoil thickness, camber and gust wavenumber on the prediction accuracy are investigated. The turbulent fluctuation with multiple wavenumber components is also considered.

To validate the accuracy of the proposed method, we also conduct numerical simulations of the airfoil–gust interactions using the advanced CAA solver that has been utilised for various aeroacoustic problems (Zhang *et al.* 2004; Ma & Zhang 2009; Gill *et al.* 2013; Liu *et al.* 2013; Wang, Hu & Zhang 2013; Gea-Aguilera, Gill & Zhang 2017; Zhong *et al.* 2018, 2019). The solver employs a high-order finite difference scheme (Ashcroft & Zhang 2003) for spatial discretisation, and uses the low-dissipation low-dispersion Runge–Kutta scheme (Hu, Hussaini & Manthey 1996) for time marching. The Euler equations are solved to yield steady mean flow fields for different airfoils, then divergence-free harmonic gusts are injected into the computational domain to interact with the airfoils. The initial location of the gusts is assigned in the buffer zones, which also prevent non-physical reflections from the boundary of the computational domain (Richards *et al.* 2004). Unsteady flow variables are recorded on an off-body integration surface as the input of a sound extrapolation solver (Zhong & Zhang 2017) to compute the far-field directivities. A generalised sound extrapolation method can also be employed for the computation of far-field directivities (Zhong & Zhang 2018*a*,*b*). In this work, all variables are non-dimensionalised, and the reference length is $L^* = c$, the reference velocity is $U^* = a_\infty$, which is the speed of sound in the far field, the reference density is $\rho^* = \rho_\infty$ and the reference pressure is $p^* = \rho_\infty a_\infty^2$.

Since a simulation of the Euler equation requires fewer assumptions (without omitting the terms in $\mathscr{E}$ or assuming the potential background mean flow), it could be viewed as more accurate. There has been experimental data of the (jet) turbulence–airfoil interaction noise (Christophe 2011). The geometry in the experiment is 3-D, and the turbulent property varies in the spanwise direction. On the contrary,

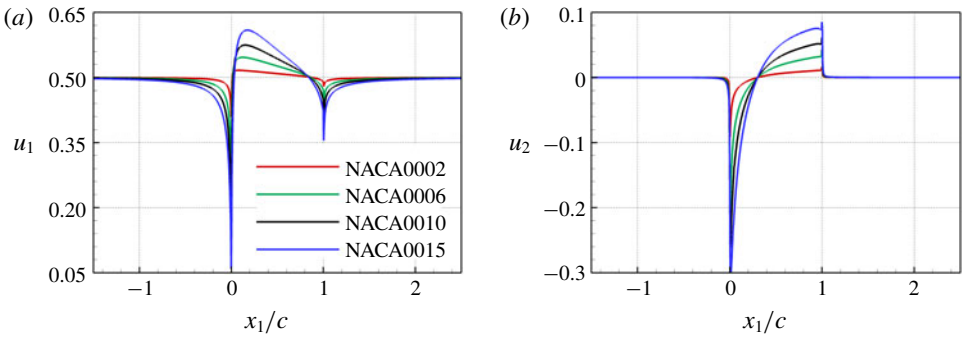


FIGURE 3. Mean flow velocities along surface streamlines ($x_2 = 0$ in the upstream free stream) of airfoils of different thickness at $M_\infty = 0.5$.

the mathematical derivation of the proposed solution is performed in the 2-D domain, being similar to Amiet's solution for the flat plate (Amiet 1976*a*). To compare the proposed result with experimental data requires the treatment of extending the 2-D data to the 3-D space (Christophe *et al.* 2009), which is essential for practical applications but is not the focus of the current study. Therefore, the validation of the proposed method is mainly based on the comparison with the high-order simulation of the Euler equations.

### 3.1. *Study of the airfoil thickness effect*

Figure 3 shows the mean flow velocities $u_1(\boldsymbol{x})$ and $u_2(\boldsymbol{x})$ along the streamline ($x_2 = 0$ in the far field, and along the airfoil surface in the near field) at $M_\infty = 0.5$. Figure 4 shows the far-field directivities for airfoils of different thickness interacting with a harmonic gust with wavelength $\lambda_g = 0.5c$ that only contains the transverse disturbance in $\boldsymbol{v}_g'$. The predictions by the flat-plate theory, the analytical corrections by the proposed method and the numerical results are presented. In the computation of the far-field directivities using the sound extrapolation method, a constant scale factor is needed to compute the far-field directivity in the sound extrapolation method (Zhong & Zhang 2017). In this section, the analytical prediction results of the NACA0002 airfoil and the numerical result are compared, and a correction factor $\mathcal{C}$, i.e. the scaled numerical value as $p_n' \to p_n'\mathcal{C}$, is obtained. The same value of $\mathcal{C}$ is applied to the numerical results of the remaining cases. It can be seen that the analytical correction can predict well the sound reduction due to airfoil thickness. The predictions match well with the numerical results for airfoils with thickness smaller than 10 %. Larger differences in $p_{rms}'$ are found for thicker airfoils. However, the proposed method can improve the prediction accuracy over the flat-plate solution. Figure 5 shows the $p_{rms}'$ distributions along the surfaces of a flat plate and a NACA0010 airfoil. The curves at different iteration steps are plotted, and close results are obtained from the first two steps. The results also suggest that there is a sound reduction effect due to the airfoil thickness, as there is a lower distribution of $p_{rms}'$ along the surface of the NACA0010 airfoil, especially near the leading edge.

Similar investigations were also conducted at $M_\infty = 0.2$, and the far-field directivity results are shown in figure 6. Sound reduction due to the airfoil thickness is also found in both upstream and downstream directions. For each airfoil, it seems that the disagreements between the numerical results and analytical predictions become

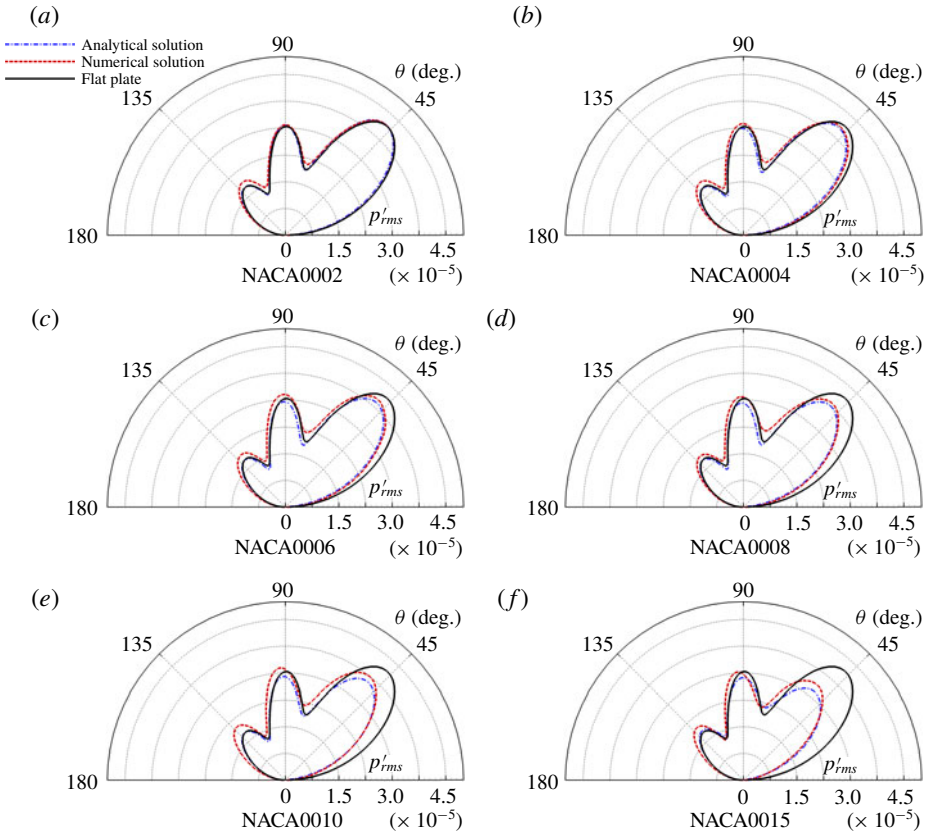


FIGURE 4. Analytical predictions of far-field $p'_{rms}$ of airfoils with different thickness interacting with a $\lambda_g = 0.5c$ gust at $M_\infty = 0.5$.

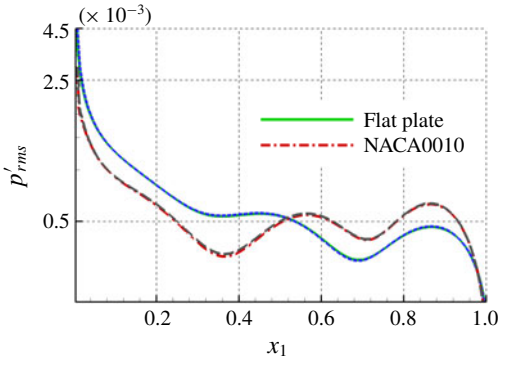


FIGURE 5. Distributions of $p'_{rms}$ on the airfoil surfaces at $M_\infty = 0.5$ and $\lambda_g = 0.5c$. Results of the first two iteration steps are shown.

smaller. The observation supports the analysis conducted in appendix A that the approximation error $\mathscr{E}$ has smaller value for lower-Mach-number cases. To measure the relative improvement in the prediction accuracy by the proposed method, we

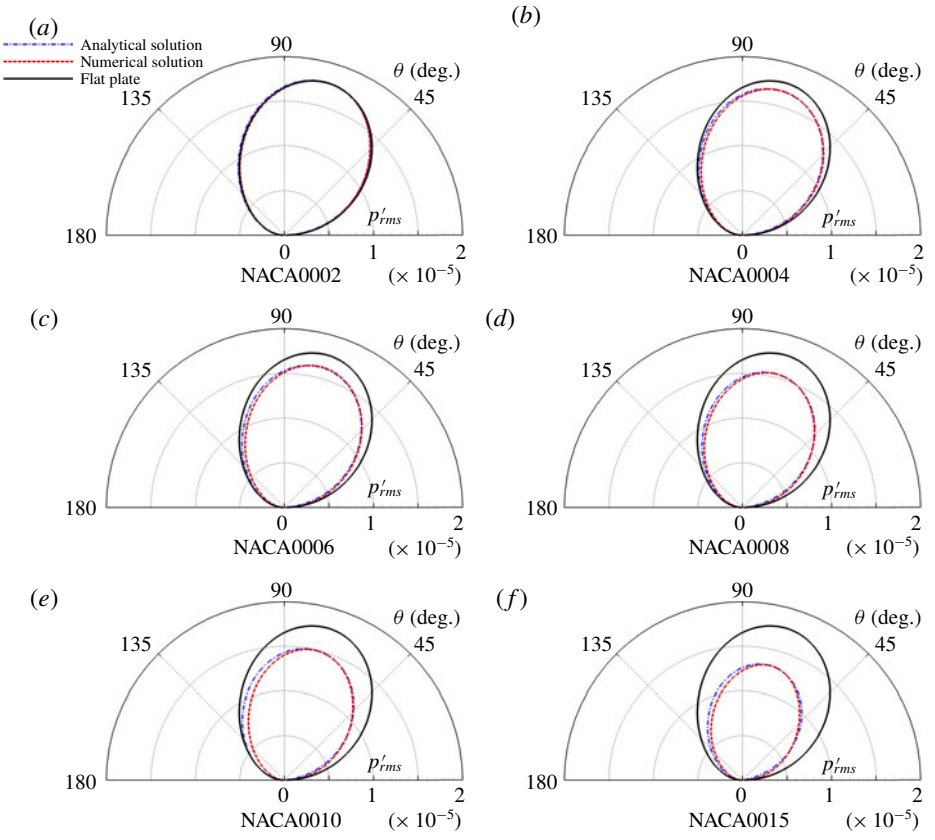


FIGURE 6. Analytical predictions of far-field $p'_{rms}$ of airfoils with different thickness interacting with a $\lambda_g = 0.5c$ gust at $M_\infty = 0.2$.

define a variable $I_r$ that is determined by the deviations of the predicted results and the numerical solutions,

$$I_r = \left[\int_0^{2\pi} |p'_c(\theta) - p'_n(\theta)|\,\mathrm{d}\theta\right] \Big/ \left[\int_0^{2\pi} |p'_f(\theta) - p'_n(\theta)|\,\mathrm{d}\theta\right], \tag{3.1}$$

where $p'_c$, $p'_f$ and $p'_n$ are the sound pressures computed by the proposed corrected solution, the flat-plate solution and the numerical simulation, respectively. Usually, a smaller value of $I_r$ suggests that the results predicted by the proposed method are closer to the CAA results than the flat-plate solution. For the cases shown in this section, the dependence of $I_r$ and airfoil thickness is shown in figure 7. For thin airfoils, both the flat-plate and the proposed solutions are close, the errors are small and $I_r \to 1$. The deviation of the prediction from the CAA results increases with the airfoil thickness, but the relative accuracy could be improved because the errors between the flat-plate solution and the CAA results are even larger.

### 3.2. *The influence of the flow Mach number*

In appendix A, we have analysed the influence of flow Mach number of the approximation error in the omitted term $\mathscr{E}$ in (2.11), and a bound for the error as a

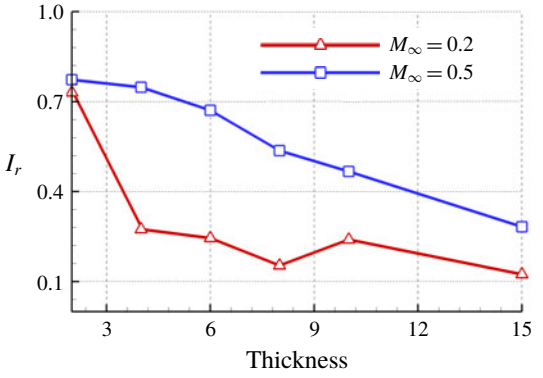


FIGURE 7. The variation of $I_r$ with the increase of airfoil thickness at $M_\infty = 0.2$ and 0.5.

function of the Mach number $M_\infty$ is proposed. However, it is difficult to propose a simple scaling law for $M_\infty$ because the acoustic responses (frequency, amplitude and radiation patterns) are changed. More importantly, the errors in the neglected terms depend on the non-uniform mean flow distributions, which are different for airfoils with varying thickness and camber. Nevertheless, we have shown that the accuracy of the proposed analytical correction is higher for the lower-Mach-number flows, which is supported by the results for airfoils at $M_\infty = 0.2$ and $M_\infty = 0.5$ in the last section. In this section, we conduct computations for the NACA0008 airfoil interacting with a gust with wavelength $\lambda_g = 0.5c$ at different $M_\infty$ (ranging from 0.15 to 0.45 with a step of 0.05) to highlight this fact. The far-field directivity results are shown in figure 8. Compared with the flat-plate solution, the sound reduction due to thickness happens in the downstream direction with increase of the Mach number. Also, it seems that the predicted results match well with the CAA solution, and the error is even smaller for the lower-Mach-number cases. The results also offer support to our observation that the predictions are fairly accurate for the airfoils with thickness smaller than 10 % in the last section.

### 3.3. *The mechanism of sound reduction due to thickness*

In the previous section, it has been shown that the leading-edge noise is reduced with the increase of airfoil thickness, and the results are consistent with the numerical simulation results. One significant difference between the proposed correction and the flat-plate solution is that the mean flow distribution is non-uniform. However, the importance of different flow components is not clear. To gain a better understanding of the roles of the mean flow velocities, we conduct computations for a NACA0012 airfoil with the following artificial mean flow distributions.

(i) Case 1: $u_1^* = u_\infty$ and $u_2^* = 0$, the effect of mean flow is not accounted for.
(ii) Case 2: $u_1^* = u_\infty$ and $u_2^* = u_2$, only the transverse non-uniformity is accounted for.
(iii) Case 3: $u_1^* = u_1$ and $u_2^* = 0$, only the streamwise non-uniformity is accounted for.
(iv) Case 4: $u_1^* = u_1$ and $u_2^* = u_2$, non-uniformities in both directions are accounted for.

Here the superscript $(\cdot)^*$ means the actual value used in the theoretical computation. The gust wavelength is $\lambda_g = 0.5c$ and the Mach numbers are $M_\infty = 0.2$ and 0.5, respectively. The predictions of the proposed method are shown in figure 9, in

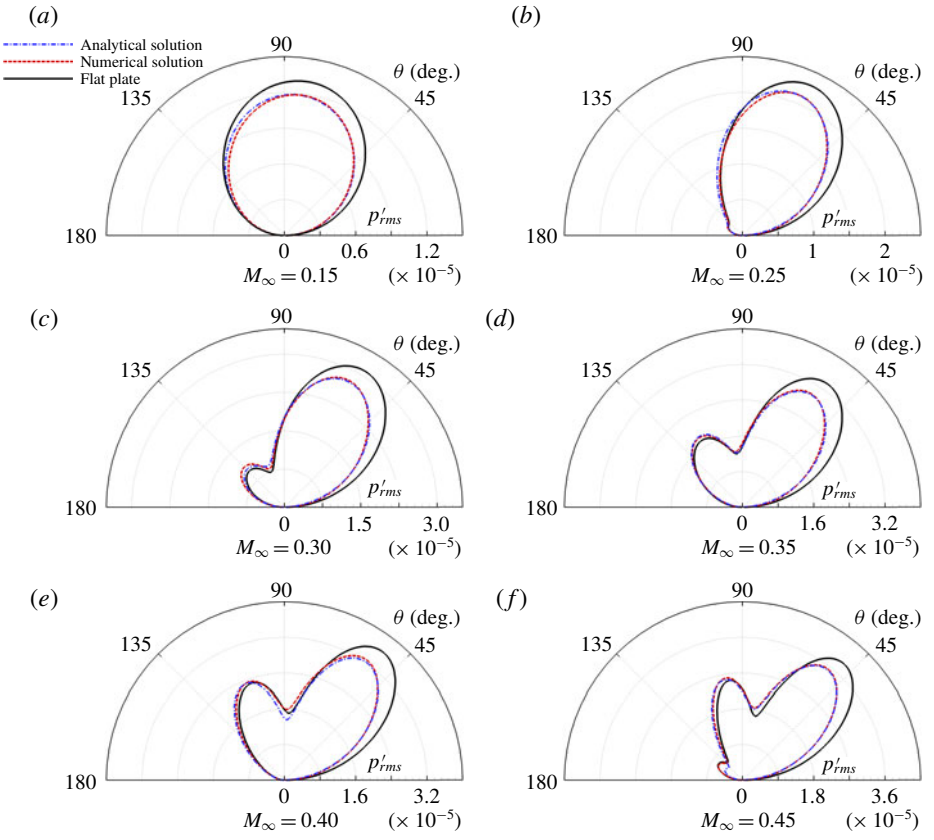


FIGURE 8. The far-field directivities of the NACA0008 airfoil interacting with $\lambda_g = 0.5c$ gusts at different Mach numbers.

which the predictions applied for a flat plate are also included. For both cases, the observer angle correction method is applied, and the angles of the radiation lobes are shifted to higher observer angles when compared with the flat-plate solution. Besides, the predictions by $u_1^* = u_\infty$ and $u_2^* = 0$ have similar amplitudes to the flat-plate computation. The thickness might lead to a slight increase in this case as shown in figure 9(*a*). However, if $u_1^* = u_1$ is used, a noticeable decrease in $p'_{rms}$ can be observed for both Mach numbers. By contrast, if either $u_1^* = u_\infty$ is uniform or $u_1^* = u_1$ is the practical value, the differences between the $u_2^* = u_2$ and $u_2^* = 0$ results are not significant. Especially for the $M_\infty = 0.2$ case, the difference caused by $u_2^*$ is negligibly small. The investigation in this section suggests that the sound reduction due to the airfoil thickness is mainly caused by the non-uniform mean flow, especially by the non-uniformity of the streamwise-direction mean flow velocity $u_1$. The results are consistent with the previous numerical simulation results (Guidati & Wagner 1999; Gill *et al.* 2013). Also, it can be seen that the results in cases 1 and 2 are close to the flat-plate solution if the semi-correction of the observer angle is not employed. Meanwhile, the (artificial) streamlines are also assigned along the airfoil surface. Therefore, we can deduce that the deflection of the streamline that is not considered in the generalised coordinate transformation has little influence on the sound prediction.

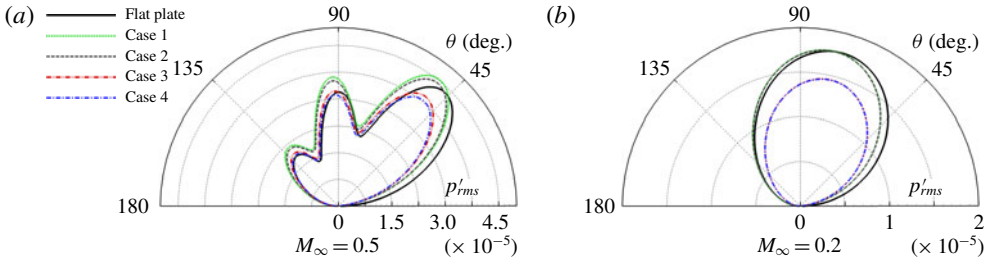


FIGURE 9. Analytical predictions of far-field $p'_{rms}$ of a NACA0012 airfoil interacting with a harmonic gust $\lambda_g = 0.5c$. Different (artificial) mean flows are employed.

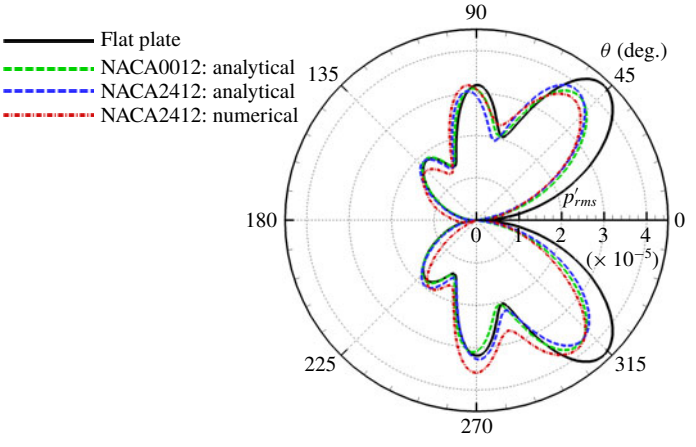


FIGURE 10. Analytical predictions of far-field $p'_{rms}$ of the cambered airfoil interacting with a harmonic gust $\lambda_g = 0.5c$ at $M_\infty = 0.5$.

### 3.4. *Applications to a cambered NACA2412 airfoil*

We also study the acoustic response of the gust to the cambered airfoil NACA2412 at $M_\infty = 0.5$. The mean flow is computed using the panel method for simplicity. The gust wavelength is $\lambda_g = 0.5c$, and the computed results are presented in figure 10. The result of the symmetric NACA0012 airfoil is also plotted. The analytical prediction can improve the accuracy over the flat-plate solution. It can be seen that the asymmetric geometry can alter the angles of radiation peaks, while the amplitude of the highest peak is comparable. The result also supports the previous observation that the sound reduction is mainly caused by the airfoil thickness (Gill *et al.* 2013). For the NACA2412 airfoil, the numerical result shows that the far-field directivity is asymmetric, which is caused by the camber that was analysed by Moreau *et al.* (2005) and verified experimentally by Devenport *et al.* (2010). However, in the proposed analytical solution, a slightly asymmetric property can be observed but is not as obvious as in the numerical simulation. One possible reason is that, in the analytical solution, we have assumed $\phi = 0$ on the $x_1$-axis ahead of the airfoil leading edge, which implicitly suggests that the sound field is antisymmetric on the pressure and suction sides. As a result, the asymmetric property caused by different mean flow distributions on the pressure and suction sides is influenced. For more generic cases, the correction method by Moreau *et al.* (2005) might be employed to account

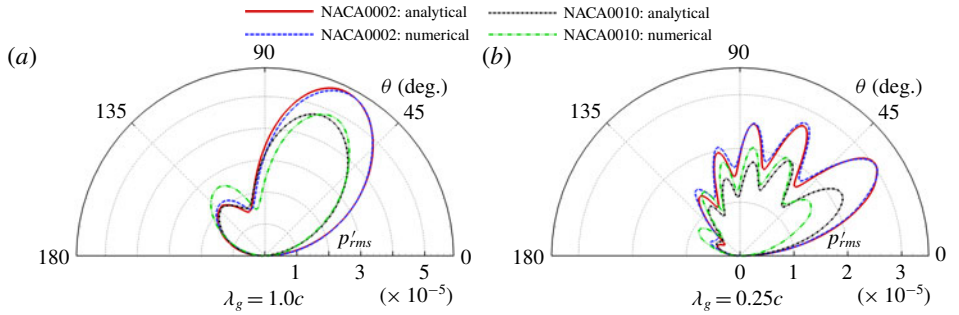


FIGURE 11. Analytical predictions of far-field $p'_{rms}$ of airfoils interacting with gusts $\lambda_g = 1.0c$ and $0.25c$ at $M_\infty = 0.5$.

for the camber effect. Nevertheless, the prediction result for the NACA2412 airfoil improves the prediction accuracy better than the flat plate ($I_r = 0.4064$ as defined in (3.1)) despite the fact that the asymmetric property is not well captured.

### 3.5. *Applications to different gust wavelengths*

In the previous section, it was shown that the proposed analytical correction method could improve the accuracy when compared with the numerical results for the cases with gust wavelength $\lambda_g = 0.5c$. In this section, the performance of the prediction method is studied for alternative gusts with $\lambda_g = 0.25c$ and $\lambda_g = 1.0c$. We focus on the NACA0002 and NACA0010 airfoils at Mach number $M_\infty = 0.5$, with angle of attack $\alpha = 0°$. Figure 11 shows the predicted far-field directivities in different configurations. In general, the predictions of the NACA0002 airfoil case match well with the numerical results. The sound reductions by the NACA0010 airfoil are captured for both gust wavelengths. However, in the upstream direction, the numerical results have larger values while the amplitudes of the radiation lobes are relatively smaller. For the higher-frequency case $\lambda_g = 0.25c$, the analytical prediction underestimates the sound reduction in the downstream direction while it overestimates the reduction at moderate to high observer angles, i.e. $\theta > 60°$. The disagreements are expected, as we have omitted some terms in the governing equations that could introduce approximation errors. As shown in appendix A, the order of the error of the term $\partial/\partial T$ is $O(M_\infty)$, suggesting that the prediction could be less accurate along with the increase of the frequency. This might be the reason why there are more noticeable differences in $p'_{rms}$ of the NACA0010 airfoil with the numerical result in the upstream direction for the $\lambda_g = 0.25c$ case. Nevertheless, much improvement is obtained compared with the flat-plate solutions. Particularly for the cases in which the NACA0010 airfoil interacts with $\lambda_g = 1.0c$ and $0.25c$ gusts, the values of $I_r$ are 0.2659 and 0.5264, respectively.

### 3.6. *Applications to oblique gusts ($k_2 \neq 0$)*

In the cases studied above, the gusts contain only the transverse disturbances ($k_2 = 0$). However, streamwise disturbances may also be present, since a harmonic gust is a Fourier component of the turbulent fluctuations. In this section, the sound radiation using an oblique gust that contains both streamwise and transverse fluctuations is studied. The vortical gust is also in the 2-D domain, and the wavenumber in the

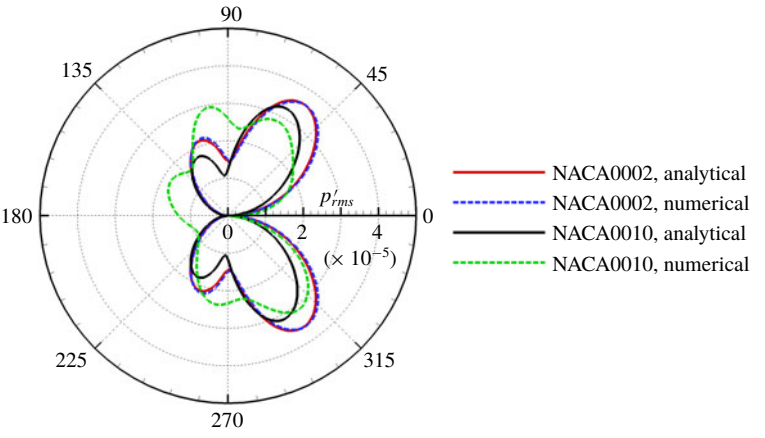


FIGURE 12. Analytical prediction of far-field $p'_{rms}$ of airfoils interacting with oblique gusts; here $M_\infty = 0.5$, $\lambda_g = 0.5c$ and $\theta_g = 45°$.

transverse direction $k_2 \neq 0$. Typically, the gust wavelength is $\lambda_g = 0.5c$ and the incident angle is $\theta_g = 45°$, i.e. the wavenumbers in both directions are $k_1 = k_2 = \sqrt{2}\pi/\lambda_g$. The Mach number is 0.5, and the NACA0002 and NACA0010 airfoils are studied for comparison.

Figure 12 shows the comparison of the predicted and numerical results for the oblique gusts. For the NACA0002 case, the predictions match reasonably well and are close to the flat-plate solution. In this case, the predicted results are equivalent to a different harmonic gust that contains only the transverse disturbance ($k_1 \to k_1/\sqrt{2}$, $A_v \to A_v/\sqrt{2}$). By contrast, the prediction of the NACA0010 airfoil by the proposed method performs badly in capturing the radiation patterns, especially on the suction side. Figure 13 shows the pressure fields by the numerical simulation using the CAA solver. For the thin airfoil NACA0002, the sound field is nearly antisymmetric on the pressure and suction sides, while a significant difference exists for the NACA0010 airfoil. In the upstream direction, the value of the sound pressure has a non-zero value, suggesting that the condition $\phi = 0$ for $x_1 < 0$ is invalid. Also, the streamwise disturbance interacting with the non-uniform mean flow may also lead to additional sound. These factors make the prediction by the analytical correction less valid for the thicker airfoils being subjected to oblique gusts. In this case, $I_r = 1.08$ for the NACA0010 airfoil, which means that the proposed analytical correction does not produce a prediction superior to the classical flat-plate solution. To have a more accurate prediction while avoiding the drawbacks of the proposed correction in this work, one may use the methods based on the RDT by Goldstein (1978) or Atassi & Grzedzinski (1989). In that case, the computation should be conducted in the 2-D domain if those more theoretically rigorous models are used.

### 3.7. *Applications to broadband cases*

In this work, we also investigate the acoustic broadband properties when the airfoils interact with the incoming turbulence. In the context of this work, the turbulence consists of gusts with different wavenumbers. For simplicity, the distribution of the amplitude of each wavenumber component is described by an isotropic Gaussian

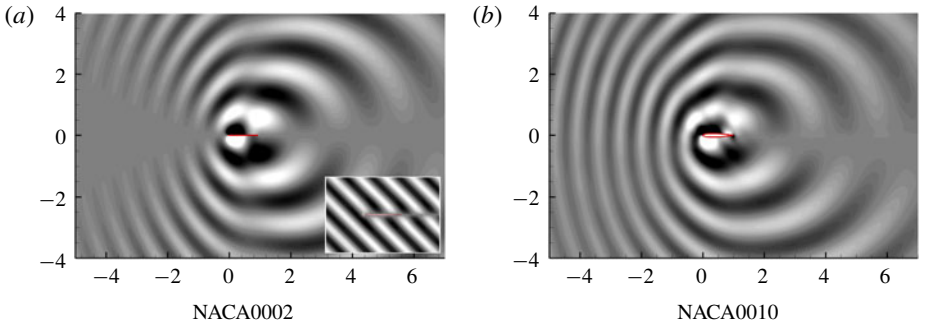


FIGURE 13. Numerical computation of $p'$ of airfoils interacting with oblique gusts (incident angle 45°, shown in the inset) at $M_\infty = 0.5$.

energy spectrum (Kraichnan 1970)

$$E(k) = \frac{2}{\pi^2} u'^2_{rms} \Lambda^4 k^3 \exp\left(-\frac{\Lambda^2 k^2}{\pi}\right), \tag{3.2}$$

where $\Lambda$ is the integral length scale, $u'_{rms}$ is the root-mean-square value of the turbulence kinetic velocity and $k = |\boldsymbol{k}| = \sqrt{k_1^2 + k_2^2}$ is the wavenumber. The velocity spectra $\Phi_{ij}(k_1, k_2)$ are calculated as (Gea-Aguilera *et al.* 2017)

$$\Phi_{ij}(k_1, k_2) = \frac{E(k)}{\pi k}\left(\delta_{ij} - \frac{k_i k_j}{k^2}\right) \quad \Rightarrow \quad \Phi_{22}(k_1, k_2) = \frac{2}{\pi^3} u'^2_{rms} \Lambda^4 k_1^2 \exp\left(-\frac{\Lambda^2 k^2}{\pi}\right). \tag{3.3}$$

The amplitude of the gust component with wavenumber $(k_1, k_2)$ is computed as $A_v(k_1, k_2) = \sqrt{\Phi_{22}(k_1, k_2)/k_1^2}$ using the divergence-free property of the gust. In this work, we set the dimensionless value $u'_{rms} = 0.01$ and $\Lambda = 0.1c$. For comparison, numerical simulations using the high-order CAA method are also conducted. In the CAA computation, the turbulent fluctuations are reproduced using an advanced synthetic turbulence method based on the digital filter approach (Gea-Aguilera *et al.* 2017).

Figure 14 shows the sound pressure distributions of the NACA0002 and NACA0012 airfoils determined by the CAA simulations. The integral length scale of the turbulence is $\Lambda = 0.1c$ and the flow Mach number is $M_\infty = 0.5$. For the NACA0012 airfoil, the sound radiation is reduced in the downstream direction, while a stronger sound distribution is observed in the upstream direction. Figure 15 shows the far-field $p'_{rms}$ of different airfoils predicted by the proposed method and by the numerical simulation. The simulation result of the NACA0002 airfoil is close to the flat-plate solution and the analytical solution. More sound reduction can be found in the downstream direction with the increase of airfoil thickness. There are apparent differences between the analytical and numerical simulation results for the real airfoils. However, the deviations are smaller than the differences between the numerical simulation and the flat-plate results. In the upstream direction, the predictions by the analytical solution are low and are close to the flat-plate solution, since we have assumed $\phi = 0$ in the upstream direction ($x_1 < 0$). By contrast, higher levels of sound to the upstream direction are found in the numerical simulations. In recent work by Zhong *et al.* (2018) and Zhong & Zhang (2019), it is shown that the streamwise

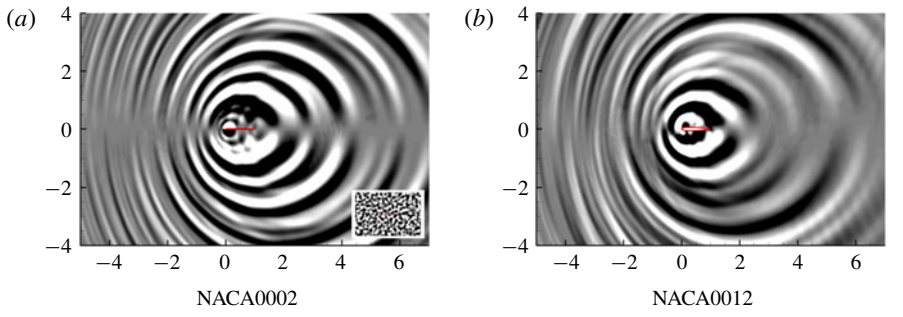


FIGURE 14. Numerical computation of $p'$ of airfoils interacting with an isotropic turbulence with $\Lambda = 0.1c$ at $M_\infty = 0.5$.

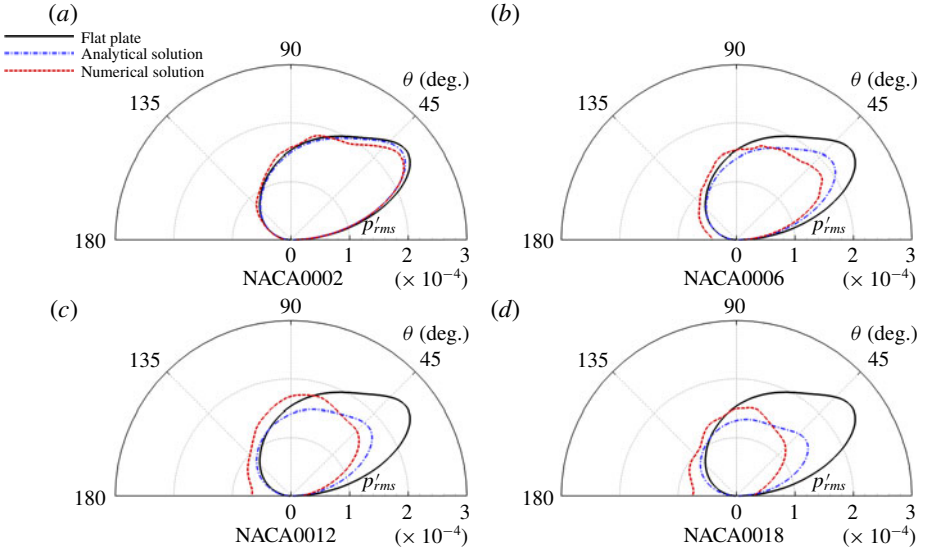


FIGURE 15. Comparisons of far-field $p'_{rms}$ obtained by the proposed correction and the numerical simulation, with $\Lambda = 0.1c$ and $M_\infty = 0.5$.

disturbance interacting with the near-field non-uniform mean flow can also contribute to sound generation in the upstream direction, which is not considered in this work. The errors are expected since reasonable approximations are made in the analytical correction, which, nevertheless, improves the prediction accuracy over the flat-plate solution.

At a lower Mach number $M_\infty = 0.2$, comparisons of far-field directivities of different airfoils are shown in figure 16. For the NACA0002 and NACA0006 airfoils, sound reduction due to the thickness is predicted and the analytical correction matches reasonably well with the numerical result. For airfoils with larger thickness, the difference in $p'_{rms}$ between the analytical solution and the numerical results becomes discernible, especially at observer angles of approximately 60°–70°. However, the errors are much smaller than those at $M_\infty = 0.5$, being consistent with the error analysis in appendix A. The error in the upstream direction is not important at this

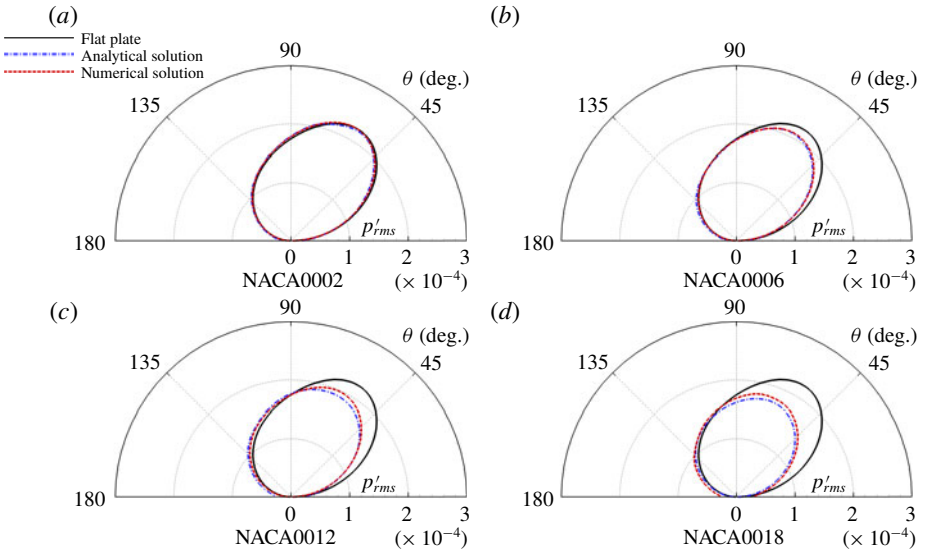


FIGURE 16. Comparisons of far-field $p'_{rms}$ obtained by the proposed correction and the numerical simulation, with $\Lambda = 0.1c$ and $M_\infty = 0.2$.

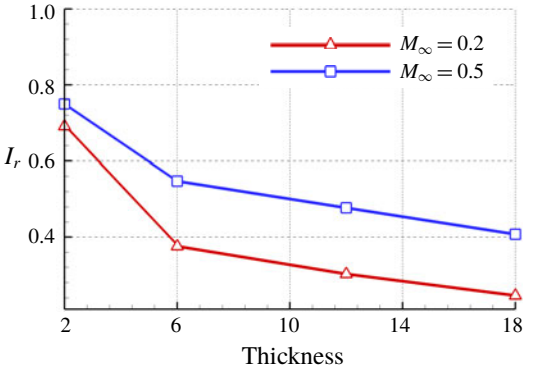


FIGURE 17. The variation of $I_r$ with the increase of airfoil thickness for the broadband cases at $M_\infty = 0.2$ and 0.5.

speed. The variations of $I_r$ with airfoil thickness are shown in figure 17, in which the improvements by the proposed method are quantitatively measured.

In this work, we also apply the proposed method to compute the acoustic responses for isotropic turbulences with Liepmann spectra (Gea-Aguilera *et al.* 2016):

$$\Phi_{11}(k_1, k_2) = \frac{2\Lambda^5 u'^2_{rms} k_2^2}{\pi^2(1+\Lambda^2 k^2)^3}, \quad \Phi_{22}(k_1, k_2) = \frac{2\Lambda^5 u'^2_{rms} k_1^2}{\pi^2(1+\Lambda^2 k^2)^3}. \tag{3.4a,b}$$

The turbulence integral length scale $\Lambda = 0.053$ is studied for the NACA0012 airfoil at $M_\infty = 0.3$ and 0.5. The numerical simulation is conducted using a new synthetic turbulence method (Shen & Zhang 2018). The comparisons of the flat-plate solution by Amiet (1975), the numerical simulation and the analytical correction method

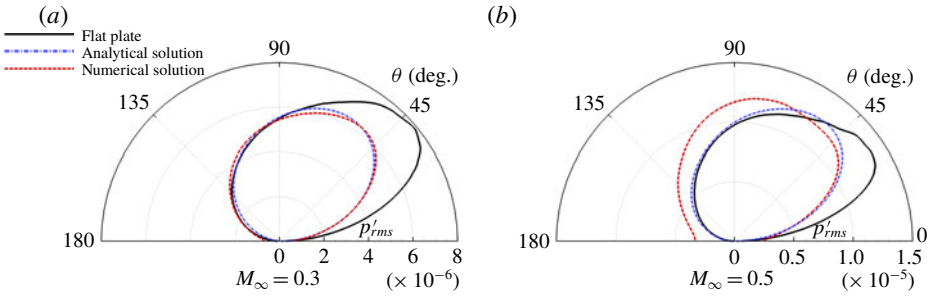


FIGURE 18. Comparisons of far-field $p'_{rms}$ for the NACA0012 airfoil obtained by the proposed correction and the numerical simulation. The turbulence has an isotropic Liepmann spectra and the integral length scale is $\Lambda = 0.053c$.

proposed in this work are shown in figure 18. For the $M_\infty = 0.3$ case, the result of the proposed analytical solution matches fairly well with the numerical result, and the sound reduction compared with the flat-plate solution is captured. For the $M_\infty = 0.5$ case, the sound reduction due to the airfoil thickness is captured in the downstream direction. In the upstream direction, the results by the flat-plate solution and the proposed correction method are close, and are lower than that by the CAA computation, being similar to the Gaussian simulation results shown in figure 15.

As for the time expense, in general, the numerical simulation takes approximately 12 h to obtain a steady mean flow, and takes another 12 h to simulate the acoustic response and to compute the far-field directivities (with ∼1.5 million grid points and ∼2 million simulation steps using 48 Intel Xeon E5-2670 processors). However, the time expense varies from case to case. For example, smaller grids are used in the NACA0002 airfoil to capture the sharp variation of the curvature at the leading edge, doubling the computational time. In the proposed solution, the calculation of a single-frequency case can be finished within 15 s, which is close to the implementation of Amiet's solution for flat plates; while the total computation time for a typical broadband case is approximately 15–20 min (with four Intel i7-4790 processors). The number for wavenumber discretisation is tested to be sufficient in this work.

## 4. Summary

An analytical correction to the flat-plate solution (Amiet 1976*a*) to compute the airfoil leading-edge noise is proposed in this work. A key step is to utilise a new space–time transformation that is analogous to the Prandtl–Glauert transformation to simplify the non-uniform sound governing equation to a classical wave equation approximately. A wave equation with three-section mixed boundary conditions is then solved using the Schwarzschild technique as in the flat-plate solution. The approximation error $\mathscr{E}$ in general increases with the flow Mach number. A semi-empirical method is also employed to account for the variation in observer angles.

The method is applied to various airfoils at different flow conditions. For simplicity, the mean flow variables employed for the analytical correction are obtained by the potential theories, and could be quickly computed from a solver based on the panel method. In the single-frequency cases, the sound reductions due to the airfoil thickness are captured, and the predictions match reasonably well with the CAA

solutions despite discernible differences. It is found that the sound reduction is mainly caused by the non-uniformity of the streamwise mean flow velocity $u_1$. The sound radiation pattern is asymmetric for a cambered airfoil, which, however, results in little difference in the overall noise emissions. There are relatively larger errors in the prediction for higher-frequency gusts. Significant differences between the analytical and numerical results are also found for the oblique gust cases. In the proposed correction of the flat-plate solution, it is assumed that the acoustic velocity potential $\phi = 0$ in the region ahead of the airfoil leading edge ($x_1 < 0$), which is incorrect as revealed by the high-fidelity numerical computation. For more accurate prediction, methods (Goldstein 1978; Atassi & Grzedzinski 1989) based on the RDT at the cost of conducting numerical simulation in a 2-D domain are needed. The analytical correction is also applied to broadband cases. At $M_\infty = 0.5$, certain prediction error exists in both upstream and downstream directions. In the upstream direction, the prediction error is probably caused by an invalid condition in the region $x_1 < 0$, and by the new sound sources due to the coupling between the gust and the non-uniform mean flow in the near field. The error in the downstream direction is probably caused by the approximation error $\mathscr{E}$ in the space–time transformation. The prediction accuracies are better for the low-Mach-number cases, as the approximation errors are small.

Nevertheless, the proposed analytical correction can improve the prediction accuracy of Amiet's flat-plate solution with only simple corrections to account for the non-uniform mean flow effect. This might therefore be a potential candidate for quick evaluation of the leading-edge noise in practical applications without conducting more expensive CAA simulations.

**Acknowledgements**

This work is supported by the National Science Foundation of China (11772282). X.H. received support from the National Science Foundation of China (91852201 and 11772005). This work was performed in the Aerodynamics, Acoustics and Noise Control Technology Centre at HKUST–Shenzhen Research Institute (SRI), PR China (see www.aantc.ust.hk).

## Appendix A. Error analysis

The governing equation (2.1) is rewritten as

$$\left(\frac{\partial}{\partial t} + u_1\frac{\partial}{\partial x_1} + u_2\frac{\partial}{\partial x_2}\right)^2 \phi - a_0^2\left(\frac{\partial^2}{\partial x_1} + \frac{\partial^2}{\partial x_2}\right)\phi = \mathscr{E}_1, \tag{A 1}$$

where

$$\mathscr{E}_1 = \frac{\boldsymbol{\nabla}\cdot(\rho_0 \boldsymbol{v}_g')}{\rho_0} - \boldsymbol{u}_0\cdot\boldsymbol{\nabla}\left(\frac{1}{a_0^2}\right)\frac{\mathrm{D}_0\phi}{\mathrm{D}_0 t} - \frac{(\boldsymbol{\nabla}\phi)\cdot\boldsymbol{\nabla}\rho_0}{\rho_0} = O(M_\infty^2)\left(\frac{\partial\phi}{\partial t},\ \boldsymbol{\nabla}\phi\right). \tag{A 2}$$

The equation can be equivalently written as

$$\frac{\partial^2\phi}{\partial t^2} + (u_1^2 - a_0^2)\frac{\partial^2\phi}{\partial x_1^2} + (u_2^2 - a_0^2)\frac{\partial^2\phi}{\partial x_2^2} + 2\left(u_1\frac{\partial^2\phi}{\partial x_1\partial t} + u_2\frac{\partial^2\phi}{\partial x_2\partial t} + u_1u_2\frac{\partial^2\phi}{\partial x_1\partial x_2}\right) + \left(u_1\frac{\partial u_2}{\partial x_1}\frac{\partial\phi}{\partial x_2} + u_2\frac{\partial u_1}{\partial x_2}\frac{\partial\phi}{\partial x_1}\right) = \mathscr{E}_1. \tag{A 3}$$

From the generalised space–time transformation defined in equation (2.6), we have

$$\frac{\partial}{\partial x_1}=f(x_1)\frac{\partial}{\partial X_1}+\Psi_1\frac{\partial}{\partial T},\quad \frac{\partial}{\partial x_2}=g(x_2)\frac{\partial}{\partial X_2}+\Psi_2\frac{\partial}{\partial T},\quad \frac{\partial}{\partial t}=\eta\frac{\partial}{\partial T}. \tag{A 4a–c}$$

Now we compute the second-order derivatives in terms of the transformed coordinates. The variables in terms of time derivative are relatively simple since

$$\frac{\partial^2}{\partial t^2}=\eta^2\frac{\partial^2}{\partial T^2},\quad \frac{\partial^2}{\partial x_1\partial t}=\eta f\frac{\partial^2}{\partial X_1\partial T}+\eta\Psi_1\frac{\partial^2}{\partial T^2},\quad \frac{\partial^2}{\partial x_2\partial t}=\eta g\frac{\partial^2}{\partial X_2\partial T}+\eta\Psi_2\frac{\partial^2}{\partial T^2}. \tag{A 5a–c}$$

The spatial derivatives are computed as

$$\begin{aligned}\frac{\partial^2}{\partial x_1^2}&=\frac{\partial}{\partial x_1}\left(f\frac{\partial}{\partial X_1}+\Psi_1\frac{\partial}{\partial T}\right)=f'\frac{\partial}{\partial X_1}+\Psi_{11}\frac{\partial}{\partial T}+f\frac{\partial}{\partial x_1}\frac{\partial}{\partial X_1}+\Psi\frac{\partial}{\partial x_1}\frac{\partial}{\partial T}\\&=f'\frac{\partial}{\partial X_1}+\Psi_{11}\frac{\partial}{\partial T}+f^2\frac{\partial^2}{\partial X_1^2}+2f\Psi_1\frac{\partial^2}{\partial X_1\partial T}+\Psi_1^2\frac{\partial^2}{\partial T^2}.\end{aligned} \tag{A 6}$$

A similar operation can be conducted for $\partial^2/\partial x_2^2$:

$$\frac{\partial^2}{\partial x_2^2}=g'\frac{\partial}{\partial X_2}+\Psi_{22}\frac{\partial}{\partial T}+g^2\frac{\partial^2}{\partial X_2^2}+2g\Psi_2\frac{\partial^2}{\partial X_2\partial T}+\Psi_2^2\frac{\partial^2}{\partial T^2}. \tag{A 7}$$

Also we have

$$\begin{aligned}\frac{\partial^2}{\partial x_1\partial x_2}&=\frac{\partial}{\partial x_2}\left(f\frac{\partial}{\partial X_1}+\Psi_1\frac{\partial}{\partial T}\right)=\Psi_{12}\frac{\partial}{\partial T}+f\frac{\partial}{\partial x_2}\frac{\partial}{\partial X_1}+\Psi_1\frac{\partial}{\partial x_2}\frac{\partial}{\partial T}\\&=\Psi_{12}\frac{\partial}{\partial T}+fg\frac{\partial^2}{\partial X_1\partial X_2}+f\Psi_2\frac{\partial^2}{\partial X_1\partial T}+g\Psi_1\frac{\partial^2}{\partial X_2\partial T}+\Psi_1\Psi_2\frac{\partial^2}{\partial T^2}.\end{aligned} \tag{A 8}$$

Then the coefficients for different derivative terms are

$$\left.\begin{aligned}&\frac{\partial^2}{\partial T^2}\colon\quad \eta^2+(u_1^2-a_0^2)\Psi_1^2+(u_2^2-a_0^2)\Psi_2^2+2(u_1\eta\Psi_1+u_2\eta\Psi_2+u_1u_2\Psi_1\Psi_2),\\&\frac{\partial^2}{\partial X_1^2}\colon\quad (u_1^2-a_0^2)f^2,\quad \frac{\partial^2}{\partial X_2^2}\colon\quad (u_2^2-a_0^2)g^2,\quad \frac{\partial^2}{\partial X_1\partial X_2}\colon\quad 2u_1u_2fg,\\&\frac{\partial^2}{\partial X_1\partial T}\colon\quad 2f\Psi_1(u_1^2-a_0^2)+2u_1\eta f,\quad \frac{\partial^2}{\partial X_2\partial T}\colon\quad 2g\Psi_2(u_2^2-a_0^2)+2u_2\eta g.\end{aligned}\right\} \tag{A 9}$$

The coefficients for the first-order derivatives are

$$\left.\begin{aligned}&\frac{\partial}{\partial T}\colon\quad (u_1^2-a_0^2)\Psi_{11}+(u_2^2-a_0^2)\Psi_{22}+2u_1u_2\Psi_{12}+u_1\frac{\partial u_2}{\partial x_1}\Psi_2+u_2\frac{\partial u_1}{\partial x_2}\Psi_1,\\&\frac{\partial}{\partial X_1}\colon\quad (u_1^2-a_0^2)f'+u_2\frac{\partial u_1}{\partial x_2}f,\quad \frac{\partial}{\partial X_2}\colon\quad (u_2^2-a_0^2)g'+u_1\frac{\partial u_2}{\partial x_1}g.\end{aligned}\right\} \tag{A 10}$$

For the space–time transformation defined in (2.6):

$$\eta=\beta_\infty,\quad f=\frac{1}{\beta_1},\quad g=\frac{1}{\beta_2},\quad \frac{\partial\Psi}{\partial x_1}=\frac{M_1}{\beta_1a_0},\quad \frac{\partial\Psi}{\partial x_2}=\frac{M_2}{\beta_2a_0}. \tag{A 11a–e}$$

For the coefficient of $\partial^2/\partial X_1\partial X_2$, the coefficient is $2u_1u_2fg$. However, in regions where one component has a large value, the other one is small. For example, in the free stream, $u_1 \to u_\infty$, the value $u_2 \to 0$. Near the leading-edge point, where $u_2$ has relatively large value, the value of $u_1$ is smaller. For this reason, we assume that these terms can be omitted, and approximation errors are therefore induced due to the non-uniform distributions of $M_1$ and $M_2$. Now we will evaluate the errors of the omitted terms.

(i) The coefficient for $\partial^2/\partial X_1\partial T$ is

$$2f\left(\frac{M_1(u_1^2-a_0^2)}{\beta_1 a_0}+\beta_\infty u_1\right)=2fu_1\left(\frac{M_1^2-1}{\beta_1}+\beta_\infty\right)=2\frac{u_1}{\beta_1}(\beta_\infty-\beta_1)\approx a_0M_1(M_1^2-M_\infty^2). \tag{A 12}$$

The order of the coefficient is $O(M_\infty^3)$ in general. For the free stream in the far field, $M_1 \to M_\infty$, so that the error tends to zero. In the region near the airfoil leading edge, $M_1 = u_1/c_0 \to 0$, so that the error term $a_0M_1(M_1^2 - M_\infty^2) \to 0$, which means that the corresponding approximation error is relatively small in that regime where the gust experiences a significant distortion.

(ii) The coefficient for $\partial^2/\partial X_2\partial T$ is

$$2g\left(\frac{M_2(u_2^2-a_0^2)}{\beta_2 a_0}+\beta_\infty u_2\right)\approx a_0M_2(M_2^2-M_\infty^2)\sim O(M_\infty^3). \tag{A 13}$$

In both the far field and in the stagnation region, $M_2 = u_2/c_0 \to 0$, so that the corresponding error tends to zero in those two regimes.

(iii) The coefficients for $\partial^2/\partial X_1^2$ and $\partial^2/\partial X_2^2$ are

$$(u_1^2-a_0^2)\frac{1}{\beta_1^2}=-a_0^2 \quad \text{and} \quad (u_2^2-a_0^2)\frac{1}{\beta_2^2}=-a_0^2. \tag{A 14a,b}$$

For isentropic flows, we can evaluate the error approximately by employing the Bernoulli equation for the mean flow variables:

$$\frac{u_\infty^2}{2}+\frac{a_\infty^2}{\gamma-1}=\frac{u_1^2+u_2^2}{2}+\frac{a_0^2}{\gamma-1} \quad \Rightarrow$$
$$a_0^2=a_\infty^2+\frac{\gamma-1}{2}(u_\infty^2-u_1^2-u_2^2)=a_\infty^2(1+O(M_\infty^2)). \tag{A 15}$$

In the far field, $u_1 \to u_\infty$ and $u_2 \to 0$, so that the error is small. By contrast, in the stagnation region, $u_1, u_2 \to 0$ and a relatively larger error is induced of the order of $O(M_\infty^2)$.

(iv) The coefficient for $\partial^2/\partial T^2$ is

$$\begin{aligned}&\beta_\infty^2-M_1^2-M_2^2+2\left(\frac{\beta_\infty}{\beta_1}M_1^2+\frac{\beta_\infty}{\beta_2}M_2^2+\frac{M_1^2M_2^2}{\beta_1\beta_2}\right)\\&\quad\approx 1-(M_\infty^2+M_1^2+M_2^2)+2\left[\left(1-\frac{M_\infty^2}{2}\right)\left(1+\frac{M_1^2}{2}\right)M_1^2\right]\\&\quad\quad+2\left[\left(1-\frac{M_\infty^2}{2}\right)\left(1+\frac{M_2^2}{2}\right)M_2^2\right]+\frac{2M_1^2M_2^2}{\beta_1\beta_2}=1+O(M_\infty^2).\end{aligned} \tag{A 16}$$

In a wide range, the mean flow Mach numbers satisfy $M_1 \to M_\infty$ and $M_2 \to 0$, which means that the error induced by the Mach numbers can be cancelled. However, around the airfoil leading edge, $M_1 \to 0$, $M_2 \to 0$, the error is of the order of $O(M_\infty^2)$.

(v) The coefficient for the term $\partial/\partial X_1$ is

$$(u_1^2 - a_0^2)f' + u_2 \frac{\partial u_1}{\partial x_2} f \approx -a_0^2 \beta_1^2 \frac{(-1)}{\beta_1^2} \frac{\partial \beta_1}{\partial x_1} + a_0^2 M_2 \frac{1}{\beta_1} \frac{\partial M_1}{\partial x_2} = \frac{a_0^2}{\beta_1} \left( M_1 \frac{\partial M_1}{\partial x_1} + M_2 \frac{\partial M_1}{\partial x_2} \right). \tag{A 17}$$

(vi) For the term $\partial/\partial X_2$, the coefficient is

$$(u_2^2 - a_0^2)g' + u_1 \frac{\partial u_2}{\partial x_1} g \approx \frac{a_0^2}{\beta_2} \left( M_1 \frac{\partial M_2}{\partial x_1} + M_2 \frac{\partial M_2}{\partial x_2} \right). \tag{A 18}$$

The induced errors are of the order of $O(M_\infty^2)$. However, in the free stream in the far field, $M_1 \to M_\infty$ and $M_2 \to 0$, which are uniform, suggesting that the two terms tend to zero due to the spatial derivatives. In the stagnation region around the leading edge, $M_1 \to 0$ and $M_2 \to 0$, so that the two error tends to zero as well.

(vii) For the term $\partial/\partial T$, from (A 10), the coefficient is

$$a_0 \left\{ M_1 M_2 \left[ \frac{\partial}{\partial x_2} \left( \frac{M_1}{\beta_1} \right) + \frac{\partial}{\partial x_1} \left( \frac{M_2}{\beta_2} \right) \right] - \beta_1^2 \frac{\partial}{\partial x_1} \left( \frac{M_1}{\beta_1} \right) - \beta_2^2 \frac{\partial}{\partial x_2} \left( \frac{M_2}{\beta_2} \right) \right\}. \tag{A 19}$$

This means that the error induced by the first-order time derivative might be as high as the same order of $O(M_\infty)$ due to the omission in the analytical solution.

In summary, the approximate equation is

$$\frac{1}{a_\infty^2} \frac{\partial^2 \phi}{\partial T^2} - \left( \frac{\partial^2 \phi}{\partial X_1^2} + \frac{\partial^2 \phi}{\partial X_2^2} \right) = \mathscr{E}. \tag{A 20}$$

The Mach-number dependence of the error terms is written as

$$\begin{aligned} \mathscr{E} = {} & O(M_\infty^2) \left( \frac{\partial \phi}{\partial t}, \nabla \phi \right) + O(M_\infty^2) \left( \frac{\partial^2 \phi}{\partial T^2} \right) + O(M_\infty^2) \left( \frac{\partial^2 \phi}{\partial X_1^2} \right) \\ & + O(M_\infty^2) \left( \frac{\partial^2 \phi}{\partial X_2^2} \right) + O(M_\infty^3) \left( \frac{\partial^2 \phi}{\partial X_1 \partial T} \right) + O(M_\infty^3) \left( \frac{\partial^2 \phi}{\partial X_2 \partial T} \right) + O(M_\infty) \left( \frac{\partial \phi}{\partial T} \right). \end{aligned} \tag{A 21}$$

Usually, the acoustic potential could be represented as $\phi(\boldsymbol{X}, T) \sim \exp(\mathrm{i}\Omega T - \mathrm{i}\boldsymbol{K} \cdot \boldsymbol{X})$. Also, the wavenumber $\boldsymbol{K}$ is proportional to the angular frequency of $\Omega \propto \omega$ due to the dispersion relation of the sound. Therefore, we could deduce that the first-order derivatives (both spatial and temporal) are proportional to the angular frequency $\omega$, while the second-order derivatives vary with $\omega^2$. Therefore, an error bound of the approximation error could be written as

$$\mathscr{E} \sim \omega O(M_\infty) + \omega O(M_\infty^2) + \omega^2 O(M_\infty^2) + \omega^2 O(M_\infty^3). \tag{A 22}$$

The analysis suggests that the analytical correction could be more accurate for flows at lower Mach number and low frequency since there is less approximation error. Also, the non-uniformity of the mean flow is reduced for thin airfoils, and the predictions are therefore more accurate.

## REFERENCES


ADAMCZYK, J. J. 1974 Passage of a swept airfoil through an oblique gust. *J. Aircraft* **11** (5), 281–287.

AMIET, R. K. 1974 Compressibility effects in unsteady thin-airfoil theory. *AIAA J.* **12** (2), 252–255.

AMIET, R. K. 1975 Acoustic radiation from an airfoil in a turbulent stream. *J. Sound Vib.* **41** (4), 407–420.

AMIET, R. K. 1976*a* High frequency thin-airfoil theory for subsonic flow. *AIAA J.* **14** (8), 1076–1082.

AMIET, R. K. 1976*b* Low-frequency approximations in unsteady small perturbation subsonic flows. *J. Fluid Mech.* **75** (3), 545–552.

AMIET, R. K. 1989 Noise produced by turbulent flow into a rotor: theory manual for noise calculation. *NASA Tech. Rep.* 181788.

AMIET, R. K. & SEARS, W. R. 1970 The aerodynamic noise of small-perturbation subsonic flows. *J. Fluid Mech.* **44** (2), 227–235.

ASHCROFT, G. & ZHANG, X. 2003 Optimized prefactored compact schemes. *J. Comput. Phys.* **190** (2), 459–477.

ATASSI, H. M. 1984 The sears problem for a lifting airfoil revisited-new results. *J. Fluid Mech.* **141**, 109–122.

ATASSI, H. M., DUSEY, M. & DAVIS, C. M. 1993*a* Acoustic radiation from a thin airfoil in non-uniform subsonic flows. *AIAA J.* **31** (1), 12–19.

ATASSI, H. M., FANG, J. & PATRICK, S. 1993*b* Direct calculation of sound radiated from bodies in nonuniform flows. *Trans. ASME J. Fluids Engng* **115** (4), 573–579.

ATASSI, H. M. & GRZEDZINSKI, J. 1989 Unsteady disturbances of streaming motions around bodies. *J. Fluid Mech.* **209**, 385–403.

ATASSI, H. M., SUBRAMANIAM, S. & SCOTT, J. 1990 Acoustic radiation from lifting airfoils in compressible subsonic flow. *AIAA Paper* 1990-3991.

AYTON, L. J. 2016 An analytic solution for gust–aerofoil interaction noise including effects of geometry. *IMA J. Appl. Maths* **82** (2), 280–304.

AYTON, L. J. & CHAITANYA, P. 2017 Analytical and experimental investigation into the effects of leading-edge radius on gust–aerofoil interaction noise. *J. Fluid Mech.* **829**, 780–808.

AYTON, L. J. & PEAKE, N. 2015 On high-frequency sound generated by gust–aerofoil interaction in shear flow. *J. Fluid Mech.* **766**, 297–325.

AYTON, L. J. & PEAKE, N. 2016 Interaction of turbulence with the leading-edge stagnation point of a thin aerofoil. *J. Fluid Mech.* **798**, 436–456.

BATCHELOR, G. K. 1967 *An Introduction to Fluid Dynamics*. Cambridge University Press.

BATCHELOR, G. K. & PROUDMAN, I. 1954 The effect of rapid distortion of a fluid in turbulent motion. *Q. J. Mech. Appl. Maths* **7** (1), 83–103.

BLANDEAU, V. P., JOSEPH, P. F., JENKINS, G. & POWLES, C. J. 2011 Comparison of sound power radiation from isolated airfoils and cascades in a turbulent flow. *J. Acoust. Soc. Am.* **129** (6), 3521–3530.

CHRISTOPHE, J. 2011 Application of hybrid methods to high frequency aeroacoustics. PhD thesis, Université libre de Bruxelles.

CHRISTOPHE, J., ANTHOINE, J. & MOREAU, S. 2009 Amiet's theory in spanwise-varying flow conditions. *AIAA J.* **47** (3), 788–790.

CRIGHTON, D. G. 1975 Basic principles of aerodynamic noise generation. *Prog. Aeronaut. Sci.* **16** (1), 31–96.

CURLE, N. 1955 The influence of solid boundaries upon aerodynamic sound. *Proc. R. Soc. Lond.* A **231** (1187), 505–514.

DEVENPORT, W. J., STAUBS, J. K. & GLEGG, S. A. L. 2010 Sound radiation from real airfoils in turbulence. *J. Sound Vib.* **329** (17), 3470–3483.

DRELA, M. 1989 *XFOIL: An Analysis and Design System for Low Reynolds Number Airfoils*. Springer.

GEA-AGUILERA, F., GILL, J. & ZHANG, X. 2017 Synthetic turbulence methods for computational aeroacoustic simulations of leading edge noise. *Comput. Fluids* **157**, 240–252.

GEA-AGUILERA, F., GILL, J., ZHANG, X., CHEN, X. X. & NODÉ-LANGLOIS, T. 2016 Leading edge noise predictions using anisotropic synthetic turbulence. *AIAA Paper* 2016-2840.

GERSHFELD, J. 2004 Leading edge noise from thick foils in turbulent flows. *J. Acoust. Soc. Am.* **116** (3), 1416–1426.

GILL, J., ZHANG, X. & JOSEPH, P. 2013 Symmetric airfoil geometry effects on leading edge noise. *J. Acoust. Soc. Am.* **134** (4), 2669–2680.

GLEGG, S. A. L., BAXTER, S. M. & GLENDINNING, A. G. 1987 The prediction of broadband noise from wind turbines. *J. Sound Vib.* **118** (2), 217–239.

GLEGG, S. A. L. & DEVENPORT, W. J. 2010 Panel methods for airfoils in turbulent flow. *J. Sound Vib.* **329** (18), 3709–3720.

GOLDSTEIN, M. E. 1978 Unsteady vortical and entropic distortions of potential flows round arbitrary obstacles. *J. Fluid Mech.* **89** (3), 433–468.

GOLDSTEIN, M. E. & ATASSI, H. M. 1976 A complete second-order theory for the unsteady flow about an airfoil due to a periodic gust. *J. Fluid Mech.* **74** (4), 741–765.

GOODWINE, B. 2010 *Engineering Differential Equations: Theory and Applications*. Springer Science & Business Media.

GUIDATI, G. & WAGNER, S. 1999 The influence of airfoil shape on gust–airfoil interaction noise in compressible flows. *AIAA Paper* 99-1843.

HALL, A. M., ATASSI, O. V., GILSON, J. & REBA, R. 2011 Effects of leading-edge thickness on high-speed airfoil–turbulence interaction noise. *AIAA Paper* 2011-2861.

HU, F. Q., HUSSAINI, M. Y. & MANTHEY, J. L. 1996 Low-dissipation and low-dispersion Runge–Kutta schemes for computational acoustics. *J. Comput. Phys.* **124** (1), 177–191.

HUNT, J. C. R. 1973 A theory of turbulent flow round two-dimensional bluff bodies. *J. Fluid Mech.* **61** (4), 625–706.

KEMP, N. H. 1952 On the lift and circulation of airfoils in some unsteady-flow problems. *J. Aero. Sci.* **19** (10), 713–714.

KERSCHEN, E. J. & BALSA, T. F. 1981 Transformation of the equation governing disturbances of a two-dimensional compressible. *AIAA J.* **19** (10), 1367–1370.

KERSCHEN, E. J. & MYERS, M. R. 1987 Perfect gas effects in compressible rapid distortion theory. *AIAA J.* **25** (3), 504–507.

KRAICHNAN, R. H. 1970 Diffusion by a random velocity field. *Phys. Fluids* **13** (1), 22–31.

LANDAHL, M. T. 1989 *Unsteady Transonic Flow*. Cambridge University Press.

LIGHTHILL, M. J. 1956 Drift. *J. Fluid Mech.* **1** (1), 31–53.

LIU, W., KIM, J. W., ZHANG, X., ANGLAND, D. & CARUELLE, B. 2013 Landing-gear noise prediction using high-order finite difference schemes. *J. Sound Vib.* **332** (14), 3517–3534.

LOCKARD, D. P. & MORRIS, P. J. 1998 Radiated noise from airfoils in realistic mean flows. *AIAA J.* **36** (6), 907–914.

LYSAK, P. D. 2011 Unsteady lift of thick airfoils in incompressible turbulent flow. PhD thesis, The Pennsylvania State University.

MA, Z. K. & ZHANG, X. 2009 Numerical investigation of broadband slat noise attenuation with acoustic liner treatment. *AIAA J.* **47** (12), 2812–2820.

MAGLIOZZI, B. 1991 Propeller and propfan noise. *NASA Tech. Rep.* 92-10599.

MARTINEZ, R. & WIDNALL, S. E. 1980 Unified aerodynamic-acoustic theory for a thin rectangular wing encountering a gust. *AIAA J.* **18** (6), 636–645.

MILES, J. W. 1950 On the compressibility correction for subsonic unsteady flow. *J. Aero. Sci.* **17** (3), 181–182.

MIOTTO, R. F., WOLF, W. R. & DE SANTANA, L. D. 2017 Numerical computation of aeroacoustic transfer functions for realistic airfoils. *J. Sound Vib.* **407**, 253–270.

MIOTTO, R. F., WOLF, W. R. & DE SANTANA, L. D. 2018 Leading-edge noise prediction of general airfoil profiles with spanwise-varying inflow conditions. *AIAA J.* **56** (5), 1711–1716.

MOREAU, S., ROGER, M. & JURDIC, V. 2005 Effect of angle of attack and airfoil shape on turbulence-interaction noise. *AIAA Paper* 2005-2973.

MORIARTY, P., GUIDATI, G. & MIGLIORE, P. 2005 Prediction of turbulent inflow and trailing-edge noise for wind turbines. *AIAA Paper* 2005-2881.

MYERS, M. R. & KERSCHEN, E. J. 1997 Influence of camber on sound generation by airfoils interacting with high-frequency gusts. *J. Fluid Mech.* **353**, 221–259.

NODE-LANGLOIS, T., WLASSOW, F., LANGUILLE, V., COLIN, Y., CARUELLE, B., GILL, J., CHEN, X. X., ZHANG, X. & PARRY, A. B. 2014 Prediction of contra-rotating open rotor broadband noise in isolated and installed configurations. *AIAA Paper* 2014-2610.

OERLEMANS, S. & MIGLIORE, P. 2004 Aeroacoustic wind tunnel tests of wind turbine airfoils. *AIAA Paper* 2004-3042.

OLSEN, W. & WAGNER, J. 1982 Effect of thickness on airfoil surface noise. *AIAA J.* **20** (3), 437–439.

OSBORNE, C. 1973 Unsteady thin-airfoil theory for subsonic flow. *AIAA J.* **11**, 205–209.

PATERSON, R. W. & AMIET, R. K. 1977 Noise and surface pressure response of an airfoil to incident turbulence. *J. Aircraft* **14** (8), 729–736.

RICHARDS, S. K., ZHANG, X., CHEN, X. X. & NELSON, P. A. 2004 The evaluation of non-reflecting boundary conditions for duct acoustic computation. *J. Sound Vib.* **270** (3), 539–557.

RIENSTRA, S. W. & HIRSCHBERG, A. 2004 *An Introduction to Acoustics*. p. 278. Eindhoven University of Technology.

ROGER, M. & MOREAU, S. 2010 Extensions and limitations of analytical airfoil broadband noise models. *Intl J. Aeroacoust.* **9** (3), 273–306.

SANTANA, L. D., CHRISTOPHE, J., SCHRAM, C. & DESMET, W. 2016 A rapid distortion theory modified turbulence spectra for semi-analytical airfoil noise prediction. *J. Sound Vib.* **383**, 349–363.

SANTANA, L. D., SCHRAM, C. & DESMET, W. 2012 Panel method for turbulence–airfoil interaction noise prediction. *AIAA Paper* 2012-2073.

SCHWARZSCHILD, K. 1901 Die Beugung und Polarisation des Lichts durch einen Spalt. I. *Math. Ann.* **55** (2), 177–247.

SCOTT, J. & ATASSI, H. 1990 Numerical solutions of the linearized Euler equations for unsteady vortical flows around lifting airfoils. *AIAA Paper* 90-0694.

SEARS, W. R. 1938 A systematic presentation of the theory of thin airfoils in non-uniform motion. PhD thesis, California Institute of Technology.

SEARS, W. R. 1941 Some aspects of non-stationary airfoil theory and its practical application. *J. Aero. Sci.* **8** (3), 104–108.

SHEN, Z. & ZHANG, X. 2018 Random-eddy superposition technique for leading edge noise predictions. *AIAA Paper* 2018-3597.

STAUBS, J. K. 2008 Real airfoil effects on leading edge noise. PhD thesis, Virginia Polytechnic Institute and State University.

TSAI, C. T. 1992 Effect of airfoil thickness on high-frequency gust interaction noise. PhD thesis, The University of Arizona.

VON KÁRMÁN, T. H. & SEARS, W. R. 1938 Airfoil theory for non-uniform motion. *J. Aero. Sci.* **5** (10), 379–390.

WANG, X., HU, Z. W. & ZHANG, X. 2013 Aeroacoustic effects of high-lift wing slat track and cut-out system. *Intl J. Aeroacoust.* **12** (3), 283–308.

ZHANG, X., CHEN, X. X., MORFEY, C. L. & NELSON, P. A. 2004 Computation of spinning modal radiation from an unflanged duct. *AIAA J.* **42** (9), 1795–1801.

ZHONG, S. Y. & ZHANG, X. 2017 A sound extrapolation method for aeroacoustics far-field prediction in presence of vortical waves. *J. Fluid Mech.* **820**, 424–450.

ZHONG, S. Y. & ZHANG, X. 2018*a* A generalized sound extrapolation method for turbulent flows. *Proc. R. Soc. Lond.* A **474** (2210), 20170614.

ZHONG, S. Y. & ZHANG, X. 2018*b* On the frequency domain formulation of the generalized sound extrapolation method. *J. Acoust. Soc. Am.* **144** (24), 24–31.

ZHONG, S. Y. & ZHANG, X. 2019 On the effect of streamwise disturbance on the airfoil–turbulence interaction noise. *J. Acoust. Soc. Am.* **145** (4), 2530–2539.

ZHONG, S. Y., ZHANG, X., GILL, J. & FATTAH, R. 2017 A numerical investigation of the airfoil–gust interaction noise in transonic flows. *AIAA Paper* 2017-3369.

ZHONG, S. Y., ZHANG, X., GILL, J., FATTAH, R. & SUN, Y. H. 2018 A numerical investigation of the airfoil–gust interaction noise in transonic flows: acoustic processes. *J. Sound Vib.* **425**, 239–256.

ZHONG, S. Y., ZHANG, X., GILL, J., FATTAH, R. & SUN, Y. H. 2019 Geometry effect on the airfoil–gust interaction noise in transonic flows. *Aero. Sci. Tech.* **92**, 181–191.